Relationships among some locally conservative discretization methods which handle discontinuous coefficients

R. A. Klausen (runhildk@ifi.uio.no)
Department of informatics and Centre of Mathematics for Applications, University of Oslo, P.O. Box 1080 Blindern, 0316 Oslo 3, Norway

T. F. Russell (thomas.russell@cudenver.edu)*
Department of Mathematics, University of Colorado at Denver, P.O. Box 173364, Campus Box 170, Denver, CO 80217-3364, U.S.A.

Abstract. This paper presents the relationships between some numerical methods suitable for a heterogeneous elliptic equation with application to reservoir simulation. The methods discussed are the classical mixed finite element method (MFEM), the control-volume mixed finite element method (CVMFEM), the support operators method (SOM), the enhanced cell-centered finite difference method (ECCFDM), and the multi-point flux-approximation (MPFA) control volume method. These methods are all locally mass conservative, and handle general irregular grids with anisotropic and heterogeneous discontinuous permeability. In addition to this, the methods have a common weak continuity in the pressure across the edges, which in some cases corresponds to Lagrange multipliers. It seems that this last property is an essential common quality for these methods.

Keywords: relationships, mixed finite element method (MFEM), expanded mixed finite element method (EMFEM), enhanced cell-centered finite difference method (ECCFDM), control-volume mixed finite element method (CVMFEM), support operator method (SOM), and multi-point flux-approximation (MPFA) control volume method.

1. Introduction

The equation discussed is

$$-\operatorname{div}(\boldsymbol{K}(\boldsymbol{x})\operatorname{grad} p) = g \text{ in } \Omega, \tag{1}$$

$$p(\boldsymbol{x}) = 0 \text{ on } \partial\Omega,$$

where Ω is a bounded horizontal domain in $\boldsymbol{R}^2$ and $\boldsymbol{K}$ is a symmetric positive-definite tensor. The boundary $\partial\Omega$ of Ω is polygonal and convex. The boundary condition is chosen for simplicity of exposition, and does not materially affect the discussion. This is to be viewed as a prototype for the pressure equation in a reservoir simulation setting.

* Partially supported by the National Science Foundation Grant Nos. DMS-0084438 and DMS-0222300.

© 2003 *Kluwer Academic Publishers. Printed in the Netherlands.*

The components of $\boldsymbol{K}$ are assumed to be bounded, but may be highly anisotropic and discontinuous, as is typical of subsurface formations with layers, fractures, faults, and so on. Equation (1) can be derived from mass conservation over a control volume and Darcy's law. The terminology is adopted from the application in mind; by p we denote the pressure, $\boldsymbol{K}$ the permeability, and $\boldsymbol{u} = -\boldsymbol{K}\,\mathrm{grad}\,p$ the Darcy velocity. In a more general setting p would be the potential and $\boldsymbol{K}$ the mobility; these generalizations are straightforward and omitted to keep the presentations as clear and simple as possible.

For this application, the discretization methods should also meet some specific demands. Engineers prefer methods that preserve the mathematical model's local mass conservation. We restrict ourselves to locally conservative methods, meaning that

- the sum of the fluxes over each cell's edges equals the accumulation term (present in transient extensions of (1)) plus any sources or sinks in the cell, and
- the flux is continuous across each edge.

In view of the geological properties discussed above, the methods of interest should be suited for

- general irregular grid,
- anisotropic permeability, and
- heterogeneous discontinuous permeability.

The methods to be discussed all fulfill these criteria, while for instance the classical Galerkin finite element method is not locally conservative. In addition we will see that the relationship between the methods also depends on a

- weak continuity in the pressure.

Locally conservative numerical methods for flows in porous media represent an active research area. Recently the journal *Computational Geosciences* published a special issue on the theme, see [1]. All the methods discussed here were represented in this special issue. The methods are the classical mixed finite element (MFEM), that for instance can be found in [2], the control-volume mixed finite element method (CVMFEM) [3], the support operator method (SOM) [4] [5], the enhanced cell-centered finite difference method (ECCFDM) [6] [7], and the multi-point flux-approximation (MPFA) control volume method [8, 9, 10, 11, 12, 13]. This is not a complete picture of all generalizations of standard cell-centered finite differences suited for reservoir

simulation on irregular grids and related situations, but those chosen can be considered as representative of the most used and discussed methods. In the special issue cited above, the papers about these or conceptually similar methods were as follows: CVMFEM [14], SOM [15], ECCFDM [16], MPFA [11, 17, 18, 19, 20]. The goal here is to present the relationships between these methods. They are all rather closely related, even if their original derivations go along quite different lines. Initially it may seem that the methods are built on quite different ideas, but the methods can be broken down and shown to be based on the same pillars.

The rest of the paper is organized as follows: In Section 3 MFEM is briefly presented, and it provides the base framework within which we formulate and relate the other methods. The mixed-hybrid finite element method (MHFEM) and associated Lagrange multipliers, which will prove useful in breaking down the other methods, are also explained. In the next section the CVMFEM is presented as a perturbation of the classical MFEM. The underlying eliminated Lagrange multipliers for this method are also pointed out. In Section 5 a finite difference method, SOM, is presented. The connection to MFEM and some of the basic properties of the method are discussed. The method in Section 6 is an enhanced cell-centered finite difference method (ECCFDM) developed from an expanded MFEM (EMFEM). The choice of approximation space in the EMFEM and the need for Lagrange multipliers are discussed. For rectangular grids and elementwise constant permeabilities, with a different choice of approximation space, the same methodology used to derive the finite difference method from the EMFEM gives rise to the MPFA method. In Section 7 the ideas behind the MPFA method and this connection to EMFEM are presented. In Section 8 a numerical example is shown that illustrates the good numerical convergence of these methods. Finally the paper is summarized.

2. Preliminaries

Let $\mathcal{L}^2$ denote the Lebesgue square-integrable functions on the domain $\Omega \subset \boldsymbol{R}^2$ with inner product $(\cdot\,,\cdot)$. Also let H^1 denote the Sobolev space of functions whose first-order derivatives are in $\mathcal{L}^2$. For vector-valued functions $\boldsymbol{v}$, define

$$H(\mathrm{div}) = \{\boldsymbol{v} \in (\mathcal{L}^2)^2 : \mathrm{div}\, \boldsymbol{v} \in \mathcal{L}^2\}.$$

We introduce the unknown fluid velocity $\boldsymbol{u}$ which gives the mixed formulation of equation (1),

$$\begin{aligned} \boldsymbol{u} &= -\boldsymbol{K}(\boldsymbol{x}) \operatorname{grad} p \qquad && \text{for } p \in H^1, \\ \operatorname{div} \boldsymbol{u} &= g && \text{for } \boldsymbol{u} \in H(\operatorname{div}). \end{aligned} \tag{2}$$

The permeability $\boldsymbol{K}$ is a symmetric positive-definite tensor, with elementwise constant components, such that for element E

$$\boldsymbol{K}^E = \begin{pmatrix} k_x^E & k_{xy}^E \\ k_{xy}^E & k_y^E \end{pmatrix}.$$

If $\{\Omega_i\}$ are subdomains of Ω such that $\bigcup \Omega_i = \Omega$, $\boldsymbol{n}$ is the outward unit normal vector on $\partial\Omega_i$, and $\boldsymbol{v}$ and p are smooth inside each Ω_i, Green's theorem gives

$$(\operatorname{grad} p, \boldsymbol{v}) = \sum_i \int_{\partial\Omega_i} \boldsymbol{v} \cdot \boldsymbol{n}\, p \, ds \;-\; (\operatorname{div} \boldsymbol{v}, p). \tag{3}$$

When $\boldsymbol{v} \cdot \boldsymbol{n}\, p$ is continuous across the boundary $\partial\Omega_i$, the first term on the right-hand side of equation (3) vanishes. If $\boldsymbol{v}$ is smooth inside each Ω_i and the normal component of $\boldsymbol{v}$ is continuous across the boundary $\partial\Omega_i$, $\boldsymbol{v} \in H(\operatorname{div})$. Likewise if p is smooth inside each Ω_i and continuous across the boundary $\partial\Omega_i$, $p \in H^1$. So when $\boldsymbol{v} \in H(\operatorname{div})$ and $p \in H^1$, the first term on the right-hand side of equation (3) is zero. Then a weak formulation of equations (2) is the problem of finding $(\boldsymbol{u}, p) \in H(\operatorname{div}) \times \mathcal{L}^2$ such that

$$\begin{aligned} (\boldsymbol{K}^{-1}\boldsymbol{u}\,, \boldsymbol{v}) - (\operatorname{div} \boldsymbol{v}, p) &= 0 \qquad && \text{for all } \boldsymbol{v} \in H(\operatorname{div}), \\ (\operatorname{div} \boldsymbol{u}, q) &= (g, q) && \text{for all } q \in \mathcal{L}^2. \end{aligned} \tag{4}$$

Note that $(\boldsymbol{K}^{-1}\boldsymbol{u}\,, \boldsymbol{v}) = (p, \operatorname{div} \boldsymbol{v})$ means that $\operatorname{grad} p = -\boldsymbol{K}^{-1}\boldsymbol{u} \in \mathcal{L}^2$ in a weak sense. So even for discontinuous $\boldsymbol{K}$ and $p \in \mathcal{L}^2$, the weak formulation in (4) gives $p \in H^1$.

The bilinear form $(\boldsymbol{K}^{-1}\cdot, \cdot)$ in (4) will be termed $a(\cdot\,, \cdot)$. Let $\mathcal{T}_h$ denote a quadrilateral element partition of Ω, where h is the maximum element diameter. Denote the set of all element edges of $\mathcal{T}_h$ by $\mathcal{E}_h$. If the grid is logically rectangular, then M and N can characterize the size of the grid such that $i = 1, \ldots, M-1$ and $j = 1 \ldots, N-1$ run over all the $(M-1)(N-1)$ interior nodes.

3. Mixed Finite Element Methods

This method uses both the velocity and the pressure as primary unknowns simultaneously. Thus, unlike finite difference or Galerkin finite element methods, MFEM directly represents the velocity with trial functions. Intuitively, this could improve the accuracy of the approximate velocity in heterogeneous problems, because the velocity is better-behaved than either the permeability or the pressure gradient when $\boldsymbol{K}$ is discontinuous. To our knowledge, there is no rigorous theory to prove this intuition, but numerical results, e.g. [21] [22], provide some supporting evidence. Another appeal of MFEM is that it is in accordance with the physics of the problem, i.e. local conservation of mass and flux continuity.

Let $H(\mathrm{div})$ be approximated by a finite-dimensional space $\boldsymbol{V}_h \subset H(\mathrm{div})$, and analogously $\mathcal{L}^2$ by $Q_h \subset \mathcal{L}^2$. The spaces $\boldsymbol{V}_h$ and Q_h are discussed in Section 3.2. The MFEM approximation of (4) is then the problem of finding $(\boldsymbol{u}_{mi}, p_{mi}) \in \boldsymbol{V}_h \times Q_h \subset H(\mathrm{div}) \times \mathcal{L}^2$ such that

$$\begin{aligned} a(\boldsymbol{u}_{mi}, \boldsymbol{v}) - (\mathrm{div}\, \boldsymbol{v}, p_{mi}) &= 0 \qquad && \text{for all } \boldsymbol{v} \in \boldsymbol{V}_h, \\ (\mathrm{div}\, \boldsymbol{u}_{mi}, q) &= (g, q) && \text{for all } q \in Q_h. \end{aligned} \tag{5}$$

Note that in this discrete setting, the analogue of the first term on the right-hand side of (3) need not vanish in the strong sense, because $\boldsymbol{v} \cdot \boldsymbol{n}$ is continuous across edges but p_{mi} is not. Dropping the term $\sum_{e \in \mathcal{E}_h} \int_e \boldsymbol{v} \cdot \boldsymbol{n}[p_{mi}]\, ds$ from (5), where $[\,\cdot\,]$ denotes the jump of a function across the edge, means that the MFEM imposes the continuity of p_{mi} across edges in a weak sense. This point will arise repeatedly in discussions of other methods.

From a mathematical point of view, MFEM is an established method with many well-known estimates on the variables. This includes superconvergence for both the velocity and pressure in case of smooth permeability and a sufficiently smooth grid; see [23] and [24]. For a more general book on MFEM, see [2]. A relationship between MFEM and cell-centered finite differences, via low-order numerical integration, was pointed out in [25]. The combination of a well-known framework and the well-established connection to cell-centered finite differences makes the MFEM a suitable reference point for the remaining methods to be considered in this paper.

The MFEM does not have an explicit flux expression, which is a favorable property when extensions to multiphase flow are to be developed. This is part of the reason for considering other methods and can explain the popularity of other methods with similar behavior.

3.1. Mixed-Hybrid FEM and Lagrange Multipliers

Another way to write the discrete form (5) is to use the original form of Green's theorem, equation (3), drop the assumption that the velocity space is a subspace of $H(\mathrm{div})$, and define a new variable λ as the pressure on the edges, viewed as a Lagrange multiplier. To ensure the needed smoothness of the velocity $\boldsymbol{u}_{mi}$, since normal components are not necessarily continuous across edges in this case, an extra equation needs to be added to (5). This form of the MFEM is often called the mixed-hybrid FEM (MHFEM). If $[\,\cdot\,]$ denotes the jump across an edge, the problem reads: find $(\boldsymbol{u}_{mi}, p_{mi}, \lambda_{mi}) \in \boldsymbol{V}_h^{-1} \times Q_h \times \Lambda_h \subset (\mathcal{L}^2)^2 \times \mathcal{L}^2 \times \mathcal{L}^2(\mathcal{E}_h)$ such that

$$\begin{aligned}
a(\boldsymbol{u}_{mi}, \boldsymbol{v}) - (\mathrm{div}\,\boldsymbol{v}, p_{mi}) + \sum_{e\in\mathcal{E}_h} \int_e [\boldsymbol{v}\cdot\boldsymbol{n}]\lambda_{mi}\,ds \;&= 0 && \\
&&& \text{for all } \boldsymbol{v} \in \boldsymbol{V}_h^{-1},\\
(\mathrm{div}\,\boldsymbol{u}_{mi}, q) = (g, q) \;&&& \text{for all } q \in Q_h,\\
\sum_{e\in\mathcal{E}_h} \int_e [\boldsymbol{u}_{mi}\cdot\boldsymbol{n}]\mu\,ds = 0 \;&&& \text{for all } \mu \in \Lambda_h.
\end{aligned}$$

This does not change the solution $(\boldsymbol{u}_{mi}, p_{mi})$, as easily can be shown. By $\boldsymbol{V}_h^{-1}$ we mean a space that does not require the continuous normal component of $\boldsymbol{V}_h$, so $\boldsymbol{V}_h^{-1}$ is part of $(\mathcal{L}^2)^2$. The space Λ_h is defined in the next subsection.

3.2. Rectangular and Quadrilateral Element Spaces

The element spaces $\boldsymbol{V}_h$ and Q_h cannot be chosen independently of each other and they are supposed to satisfy a discrete inf-sup condition, known as the **Babuška-Brezzi condition**,

$$\sup_{\boldsymbol{v}\in\boldsymbol{V}_h} \frac{(q, \mathrm{div}\,\boldsymbol{v})}{\|\boldsymbol{v}\|_{H(\mathrm{div})}} \geq \beta\|q\| \qquad \text{for all } q \in Q_h, \tag{6}$$

where $\beta > 0$ is independent of h and $\|\cdot\|$ denotes the $\mathcal{L}^2$ norm. In addition, we assume that

$$\|\boldsymbol{v}\|_{H(\mathrm{div})} \leq c\|\boldsymbol{v}\| \quad \text{for all } \boldsymbol{v} \in Z_h = \{\boldsymbol{v} \in \boldsymbol{V}_h : (\mathrm{div}\,\boldsymbol{v}, q) = 0, q \in Q_h\}. \tag{7}$$

The conditions (6) and (7) are important tools in analysis of MFEM and are necessary to ensure stability. One possible choice for $\boldsymbol{V}_h$ and Q_h is the lowest-order Raviart-Thomas element, denoted by $\boldsymbol{RT}_0$ [26]. For rectangular elements this can be defined as

$$\boldsymbol{RT}_{0,r}(E) := (P_0(E) + P_0(E)x) \times (P_0(E) + P_0(E)y),$$

with P_0 a polynomial of order zero; this gives

$$\boldsymbol{V}_{h,r} := \{\boldsymbol{v} \in H(\mathrm{div}) : \ \boldsymbol{v}|_E \in \boldsymbol{RT}_{0,r}(E), E \in \mathcal{T}_h\}$$

and

$$Q_{h,r} = Q_h := \{q \in \mathcal{L}^2 : \ q|_E \in P_0(E), E \in \mathcal{T}_h\}.$$

The Lagrange multiplier space on the edges is

$$\Lambda_{h,r} = \Lambda_h := \{\mu \in \mathcal{L}^2(\mathcal{E}_h) : \ \mu|_e \in P_0(e), e \in \mathcal{E}_h\}.$$

The velocity space has continuous normal component across each edge, and in the piecewise-constant pressure space the characteristic test function of each cell enforces local mass conservation on that cell.

For the geologically irregular subsurface applications in mind, the grids may need to have general convex quadrilateral elements. The Raviart-Thomas space over quadrilateral elements is defined with help of a reference square element $\hat{E}$. For any element $E \in \mathcal{T}_h$, $F^E : \hat{E} \longrightarrow E$ is an invertible bilinear mapping. Let $\boldsymbol{D}$ be the Jacobian matrix and J the Jacobian. Let $\boldsymbol{x}_i = (x_i, y_i)$, $i = 1, 2, 3, 4$, be the four vertices of element E in a counterclockwise direction. If $\hat{\boldsymbol{x}}_1 = (0, 0)^T$, $\hat{\boldsymbol{x}}_2 = (1, 0)^T$, $\hat{\boldsymbol{x}}_3 = (1, 1)^T$, and $\hat{\boldsymbol{x}}_4 = (0, 1)^T$, then

$$F^E(\hat{x}, \hat{y}) = \boldsymbol{x}_1 + \boldsymbol{x}_{21}\hat{x} + \boldsymbol{x}_{41}\hat{y} + (\boldsymbol{x}_{32} - \boldsymbol{x}_{41})\hat{x}\hat{y}$$

for $\boldsymbol{x}_{ij} = \boldsymbol{x}_i - \boldsymbol{x}_j$. Scalar functions transform from $\hat{E}$ to E in the obvious way, but vector functions require the **Piola transform** $\mathcal{P}^E$ that preserves normal components (fluxes), enabling $\boldsymbol{V}_h \subset H(\mathrm{div})$ [2]. This is defined by

$$\boldsymbol{u} = \mathcal{P}^E\hat{\boldsymbol{u}} = \frac{1}{J}\boldsymbol{D}\hat{\boldsymbol{u}}.$$

The lowest-order Raviart-Thomas element over a quadrilateral is defined by

$$\boldsymbol{V}_h = \boldsymbol{RT}_0 := \{\boldsymbol{v}(\boldsymbol{x}) = \mathcal{P}^E\hat{\boldsymbol{v}} \circ (F^E)^{-1}(\boldsymbol{x}) : \ \hat{\boldsymbol{v}} \in \boldsymbol{V}_{h,r}\}.$$

The definition of Q_h and Λ_h is the same on a quadrilateral grid as on rectangular grids.

Some more care has to be taken when working with quadrilateral elements compared to triangular or rectangular elements. This is due to the fact that the Jacobian of F^E, J, is not constant. This means for instance that $\mathrm{div}(\boldsymbol{V}_h) \not\subset Q_h$. In [23] both stability and the conditions (6) and (7) are shown for MFEM with the above definition of $\boldsymbol{V}_h$ and Q_h on quadrilateral elements. It should also be noted that these results apply only to the two-dimensional (2D) case, in which $\boldsymbol{RT}_0$ as defined here contains the constant vector fields and therefore passes the "patch test" [27]. For analogous hexahedral elements (trilinear images of a

reference cube) in $\boldsymbol{R}^3$, the Piola-transformed $\boldsymbol{RT}_0$ does not contain the constant vectors, so that the theoretical situation is uncertain [14].

3.3. $\boldsymbol{K}$ AND $\boldsymbol{K}^{-1}$ METHODS

This subsection divides the methods considered in this paper into two classes, as discussed in [28]. As seen in the weak form (4), if we let $\boldsymbol{f}$ denote the Darcy flux vector, the MFEM essentially reduces Darcy's law to a relationship of the form

$$\boldsymbol{K}^{-1}\boldsymbol{f} = -\delta p, \tag{8}$$

where δp denotes a pressure difference. $\boldsymbol{K}^{-1}$ appears discretely as a mass matrix, so that a combination of fluxes equals a pressure drop. We therefore consider MFEM to belong to the class of "$\boldsymbol{K}^{-1}$ methods," in which there are explicit expressions for pressure drops in terms of fluxes, but not conversely. The methods discussed in Sections 4 (CVMFEM) and 5 (SOM) are also of this type. When $\boldsymbol{K}$ is discontinuous in 1D, the standard harmonic mean (see (25)) follows easily from numerical integration in $\boldsymbol{K}^{-1}$ methods.

The alternative perspective of "$\boldsymbol{K}$ methods" is based on

$$\boldsymbol{f} = -\boldsymbol{K}\delta p, \tag{9}$$

instead of (8), with a combination of pressure drops equaling a flux. This type is represented in Sections 6 (EMFEM, ECCFDM) and 7 (MPFA). With explicit flux expressions in terms of pressures, the $\boldsymbol{K}$ methods are more easily viewed as extensions of standard cell-centered finite-difference or finite-volume methods, and hence are more compatible with traditional codes and solvers than $\boldsymbol{K}^{-1}$ methods are. On the other hand, $\boldsymbol{K}$ methods may require enhancement to recover the 1D harmonic mean and attain optimal-order accuracy (ECCFDM), or may be subject to tighter constraints on geometry and anisotropy than $\boldsymbol{K}^{-1}$ methods in order to maintain monotonicity and stability (MPFA, [19], [29]).

One can consider relating the two classes of methods by inverting $\boldsymbol{K}^{-1}$ in (8) to obtain (9). For MFEM/CVMFEM and the MPFA O-method on a uniform 2D grid of parallelograms, this was done in [28]. To make the $\boldsymbol{K}$ of (9) sparse, $\boldsymbol{K}^{-1}$ was partially lumped and incompletely inverted. The comparison suggested that the methods would differ more with increasing aspect ratio or non-orthogonality. This is qualitatively consistent with the results of [29] and the theoretical optimal-order convergence of MFEM on parallelogram grids [2]. We do not pursue this inversion approach further in this paper.

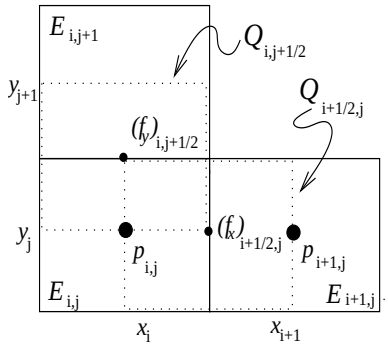

Figure 1. Cells, unknowns, and control volumes for rectangular CVMFEM

4. Control Volume Mixed Finite Element Method

The Control Volume Mixed Finite Element Method (CVMFEM) can be considered as both a control volume method, and as a mixed finite element method. The first presentation of the method, given in [3], describes it as a control volume method in an integral setting. We present this briefly here for a rectangular grid. The pressure equation, and the pressure trial and test space Q_h, are the same as for the rectangular MFEM in Section 3.2. The velocity trial space $\boldsymbol{RT}_{0,r}$ is also the same, but the velocity test space is different. Assume (for this rectangular case) that $\boldsymbol{K}$ is a diagonal tensor, and write the x-component of the Darcy equation in (2) in the form

$$k_x^{-1} u_x + \frac{\partial p}{\partial x} = 0, \tag{10}$$

where $\boldsymbol{u} = (u_x, u_y)$. Integrate (10) over the control volume $Q_{i+1/2,j} = (x_i, x_{i+1}) \times (y_{j-1/2}, y_{j+1/2})$, as depicted in Figure 1. This is equivalent to integrating the scalar product of the Darcy equation with the piecewise-constant test function

$$\boldsymbol{v}_{i+1/2,j}(\boldsymbol{x}) = \begin{cases} (1,0) & \text{if } \boldsymbol{x} \in Q_{i+1/2,j}, \\ (0,0) & \text{if } \boldsymbol{x} \notin Q_{i+1/2,j}. \end{cases} \tag{11}$$

Integrating out the x-derivative of p, we obtain

$$(\boldsymbol{K}^{-1} \boldsymbol{u}_{cm}, \boldsymbol{v}_{i+1/2,j}) + \int_{y_{j-1/2}}^{y_{j+1/2}} (p_{cm}(x_{i+1}, y) - p_{cm}(x_i, y))\, dy = 0. \tag{12}$$

In an analogous manner, for volume $Q_{i,j+1/2}$ in Figure 1 and test function

$$\boldsymbol{v}_{i,j+1/2}(\boldsymbol{x}) = \begin{cases} (0,1) & \text{if } \boldsymbol{x} \in Q_{i,j+1/2}, \\ (0,0) & \text{if } \boldsymbol{x} \notin Q_{i,j+1/2}, \end{cases} \tag{13}$$

we have

$$(\boldsymbol{K}^{-1}\boldsymbol{u}_{cm}, \boldsymbol{v}_{i,j+1/2}) + \int_{x_{i-1/2}}^{x_{i+1/2}} (p_{cm}(x, y_{j+1}) - p_{cm}(x, y_j))\, dx = 0. \quad (14)$$

In (12) and (14), we have discrete forms of Darcy's law on velocity control volumes, relating the velocity $\boldsymbol{u}$ to the pressure difference between the two ends. The pressure difference results from integrating out the pressure derivative, analogous to the integration by parts in Section 3 that obtains $-(\operatorname{div} \boldsymbol{v}, p_{mi})$ from $(\boldsymbol{v}, \operatorname{grad} p_{mi})$. The analogue of $\operatorname{div} \boldsymbol{v}$ is a δ-distribution on two opposite edges of $Q_{i+1/2,j}$ or $Q_{i,j+1/2}$.

Since the connection to mixed finite element methods fits better with the setting here, see [30], this approach will be used. The velocity test function can be viewed as belonging to the image of a mapping from $\boldsymbol{RT}_{0,r}$ onto a new space

$$\begin{aligned}\boldsymbol{Y}_h = \{(v_x, v_y) : {} & v_x \text{ is piecewise constant on volumes } Q_{i+1/2,j}, \\ & v_y \text{ is piecewise constant on volumes } Q_{i,j+1/2}\}.\end{aligned}$$

The mapping $\gamma_h : \boldsymbol{V}_h \longrightarrow \boldsymbol{Y}_h$ preserves fluxes across edges, i.e.,

$$\gamma_h(\boldsymbol{v}) = \sum_{i,j} [v_x(x_{i+1/2}, y_j)\boldsymbol{v}_{i+1/2,j} + v_y(x_i, y_{j+1/2})\boldsymbol{v}_{i,j+1/2}], \quad (15)$$

where $\boldsymbol{v} = (v_x, v_y)$. To obtain the p integrals in (12) and (14) from a bilinear form, the appropriate analogue of $(\operatorname{div} \boldsymbol{v}, p_{mi})$ is

$$\begin{aligned} b(\boldsymbol{v}, p) \;=\; \sum_{i,j} \Bigg[& v_x(x_{i+1/2}, y_j) \int_{y_{j-1/2}}^{y_{j+1/2}} (p(x_i, y) - p(x_{i+1}, y))\, dy \\ & + v_y(x_i, y_{j+1/2}) \int_{x_{i-1/2}}^{x_{i+1/2}} (p(x, y_j) - p(x, y_{j+1}))\, dx \Bigg] \end{aligned} \quad (16)$$

Then the CVMFEM is to find $(\boldsymbol{u}_{cm}, p_{cm}) \in \boldsymbol{V}_{h,r} \times Q_{h,r} \subset H(\operatorname{div}) \times \mathcal{L}^2$ such that

$$\begin{aligned} a(\boldsymbol{u}_{cm}, \gamma_h \boldsymbol{v}) - b(\gamma_h \boldsymbol{v}, p_{cm}) &= 0 \qquad \text{for all } \boldsymbol{v} \in \boldsymbol{V}_h, \\ (\operatorname{div} \boldsymbol{u}_{cm}, q) &= (g, q) \qquad \text{for all } q \in Q_h. \end{aligned} \quad (17)$$

The definition of the CVMFEM on quadrilaterals is a generalization of the above development. Figure 2 shows the support $Q_{i+1/2,j}$ of the test function $\boldsymbol{v}_{i+1/2,j}$ analogous to the one in (11). This is the union of two cell halves, $Q_{i+1/4,j} = F_{i,j}^E([\frac{1}{2}, 1] \times [0, 1])$ and $Q_{i+3/4,j} = F_{i+1,j}^E([0, \frac{1}{2}] \times [0, 1])$, in the notation of Section 3.2. The corresponding basis test function is defined by

$$\boldsymbol{v}_{i+1/2,j}\left(F_{i,j}^E(\hat{x}, \hat{y})\right) = \frac{1}{J_{i,j}(\hat{x}, \hat{y})} (\boldsymbol{D}_{i,j}^E(\hat{x}, \hat{y})) \begin{pmatrix} 1 \\ 0 \end{pmatrix},$$

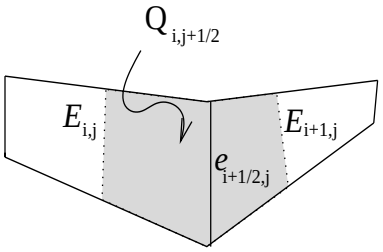

Figure 2. Two adjacent gridcells, and the area of support for the velocity function, $Q_{i,j+1/2}$

for $\frac{1}{2} \le \hat{x} \le 1,\ 0 \le \hat{y} \le 1$, and

$$\boldsymbol{v}_{i+1/2,j}\left(F^E_{i+1,j}(\hat{x},\hat{y})\right) = \frac{1}{J_{i+1,j}(\hat{x},\hat{y})}(\boldsymbol{D}^E_{i+1,j}(\hat{x},\hat{y}))\begin{pmatrix}1\\0\end{pmatrix},$$

for $0 \le \hat{x} \le \frac{1}{2},\ 0 \le \hat{y} \le 1$. The crucial analogue of integration by parts is

$$\begin{aligned}
&\int_{Q_{i+1/2,j}} \operatorname{grad} p \cdot \boldsymbol{v}_{i+1/2,j}\, dx\, dy \\
&= \int_{Q_{i+1/4,j}} \frac{1}{J_{i,j}(\hat{x},\hat{y})} \begin{pmatrix} \frac{\partial p}{\partial x} & \frac{\partial p}{\partial y} \end{pmatrix} \cdot \begin{pmatrix} \frac{\partial x}{\partial \hat{x}} & \frac{\partial y}{\partial \hat{x}} \end{pmatrix}^T \Big|_{Q_{i+1/4,j}} dx\, dy \\
&\qquad + \int_{Q_{i+3/4,j}} \frac{1}{J_{i+1,j}(\hat{x},\hat{y})} \begin{pmatrix} \frac{\partial p}{\partial x} & \frac{\partial p}{\partial y} \end{pmatrix} \cdot \begin{pmatrix} \frac{\partial x}{\partial \hat{x}} & \frac{\partial y}{\partial \hat{x}} \end{pmatrix}^T \Big|_{Q_{i+3/4,j}} dx\, dy \\
&= \int_0^1 \int_{1/2}^1 \frac{\partial p}{\partial \hat{x}}\Big|_{Q_{i+1/4,j}} d\hat{x}\, d\hat{y} + \int_0^1 \int_0^{1/2} \frac{\partial p}{\partial \hat{x}}\Big|_{Q_{i+3/4,j}} d\hat{x}\, d\hat{y} \\
&= \int_0^1 (p|_{\hat{x}=1} - p|_{\hat{x}=1/2})\Big|_{Q_{i+1/4,j}} d\hat{y} + \int_0^1 (p|_{\hat{x}=1/2} - p|_{\hat{x}=0})\Big|_{Q_{i+3/4,j}} d\hat{y} \\
&= \int_0^1 p|_{\hat{x}=1/2}\, d\hat{y}\Big|_{Q_{i+3/4,j}} - \int_0^1 p|_{\hat{x}=1/2}\, d\hat{y}\Big|_{Q_{i+1/4,j}} \\
&\approx p_{i+1,j} - p_{i,j}, \qquad (18)
\end{aligned}$$

where we note the cancellation of p at the edge $e_{i+1/2,j}$ between the two halves of $Q_{i+1/2,j}$. This is equivalent to an elimination of the Lagrange multipliers of Section 3.1 and will be related to corresponding developments in other methods. In effect, a weak continuity in the pressure has been obtained via the choice of test function, such that $\int_{e_{i+1/2,j}} [p]\, ds = 0$ in (18).

5. The Support Operator Method

The Support Operator Method, SOM [31], is used to give a finite difference-like approximation. The key is the approximation of the operators div and $-\boldsymbol{K}$ grad, and the adjoint relationship of these operators and their approximations in suitable continuous and discrete inner products. In [31] the parabolic case is solved, with an additional time-dependent term that is discretized by a backward finite difference. The conservation equation and Darcy's law are approximated separately, as for the rest of the methods discussed in this paper. A well-conditioned mass matrix is derived by eliminating the pressure to obtain an equation in the discrete flux. The method from [31] is expanded in [5] to cover a full permeability tensor.

The elliptic case will be described here. The discrete SOM is defined via the operators $\mathcal{D}$ and $\mathcal{G}$, respectively analogues of div and $-\boldsymbol{K}$ grad, as

$$\begin{aligned} \boldsymbol{u}_{so} &= \mathcal{G} p_{so}, \\ \mathcal{D}\boldsymbol{u}_{so} &= G. \end{aligned} \tag{19}$$

SOM is outlined here directly in the discrete spaces, with details in Appendix A. The discrete scalar (pressure) function space is termed HC and is cell-centered, and $\mathcal{HS}$ denotes the discrete edge-centered vector (velocity) space, whose functions are evaluated via normal components (fluxes). For each discrete space, two inner products are defined. The first, the **natural** inner product, is a discrete analogue of the $\mathcal{L}^2$ inner product for the scalar functions and of the energy inner product, $a(\cdot,\cdot) = (\boldsymbol{K}^{-1}\cdot,\cdot)$, for vector functions. For HC, this is

$$(p,q)_{\mathrm{HC}} = \sum_{E\in\mathcal{T}_h} p^E q^E A^E,$$

where A^E is the area of the element E and p^E, q^E are the discrete cell-centered function values in E. For $\mathcal{HS}$, it is

$$(\boldsymbol{A},\boldsymbol{B})_{\mathcal{HS}} = \sum_{E\in\mathcal{T}_h} \sum_{v} (\boldsymbol{A},\boldsymbol{B})_v^E A_v^E,$$

where v runs over the vertices of E, A_v^E is an area such that $\sum_v A_v^E = A^E$, and $(\boldsymbol{A},\boldsymbol{B})_v^E$ is a discrete vector multiplication that includes the permeability. For details, and the second **formal** inner products for each space, see Appendix A. The main assumption from which the operators are derived is the existence of an adjoint operator $\mathcal{D}^*$ such that

$$(\mathcal{D}\boldsymbol{u}, p)_{\mathrm{HC}} = (\boldsymbol{u}, \mathcal{D}^* p)_{\mathcal{HS}}. \tag{20}$$

The key is that $\mathcal{D}^*$ equals $\mathcal{G}$, the approximation of $-\boldsymbol{K}\,\mathrm{grad}$, so that equation (20) can be considered as an approximation of

$$\int_\Omega \mathrm{div}\,\boldsymbol{u}\,p\,d\boldsymbol{x} = -\int_\Omega (\boldsymbol{K}^{-1}\boldsymbol{u})^T\boldsymbol{K}\,\mathrm{grad}\,p\,d\boldsymbol{x} = -\int_\Omega \boldsymbol{u}\,\mathrm{grad}\,p\,d\boldsymbol{x},$$

interpreting $(\cdot,\cdot)_{\mathrm{HC}}$ and $(\cdot,\cdot)_{\mathcal{HS}}$ as numerical integrations.

In relation to the classical MFEM, this is analogous to dropping the term $\sum_{e\in\mathcal{E}_h}\int_e \boldsymbol{v}\cdot\boldsymbol{n}[p_{mi}]\,ds$ from the integration by parts that leads to (5). In the CVMFEM, the corresponding term is dropped by the cancellation of edge pressures in the derivation (18), which is that method's equivalent of integration by parts. In the SOM, (20) states that the operators and inner products are defined such that the dropped term does not arise. All of these formulations therefore impose a weak continuity on the pressure, and in the framework of the MHFEM, they set the Lagrange multiplier term to be zero.

5.1. The Support Operator Method Derived from Mixed Finite Element Method

Instead of deriving SOM as in [31], one can start from the MFEM formulation with the lowest-order Raviart-Thomas elements and numerical integration. In [4], this relationship to MFEM is used to prove convergence of SOM in the case of smooth permeability. The numerical integration can be formulated as a perturbation $a_h(\cdot,\cdot)$ of $a(\cdot,\cdot)$. The first equation of (19) is actually defined in terms of operators $\mathcal{S}$, $\mathcal{D}'$ and $\mathcal{M}$, such that $\boldsymbol{u}_{so} = \mathcal{G}p_{so}$ is written as $\mathcal{S}\boldsymbol{u}_{so} = \mathcal{D}'\mathcal{M}p_{so}$, where $\mathcal{G}{=}\mathcal{S}^{-1}\mathcal{D}'\mathcal{M}$; see Appendix A for details. $\mathcal{D}'$ approximates grad and is the adjoint of $\mathcal{D}$ in the formal inner product, while $\mathcal{S}$ and $\mathcal{M}$ approximate $\boldsymbol{K}^{-1}$ and the identity, respectively, and both contain geometric factors that transform between the natural and formal inner products. Note that SOM does not offer an explicit discrete velocity (or flux) expression; the inversion of $\mathcal{S}$ gives a non-local flux approximation.

Define the subspaces $\boldsymbol{V}_h^x$ and $\boldsymbol{V}_h^y$ of $\boldsymbol{V}_h$ associated with the logically vertical x-edges $(i+1/2,j)$ and the logically horizontal y-edges $(i,j+1/2)$, respectively, of $\mathcal{T}_h$. The SOM can be formulated as follows: find $(\boldsymbol{u}_{so},p_{so})\in\boldsymbol{V}_h\times Q_h$ such that

$$\begin{aligned} a_h(\boldsymbol{u}_{so},\boldsymbol{v}_x)+(p_{so},\mathrm{div}\,\boldsymbol{v}_x) &= 0 && \text{for all } \boldsymbol{v}_x\in\boldsymbol{V}_h^x,\\ a_h(\boldsymbol{u}_{so},\boldsymbol{v}_y)+(p_{so},\mathrm{div}\,\boldsymbol{v}_y) &= 0 && \text{for all } \boldsymbol{v}_y\in\boldsymbol{V}_h^y,\\ (\mathrm{div}\,\boldsymbol{u}_{so},q) &= (g,q) && \text{for all } q\in Q_h, \end{aligned} \qquad (21)$$

where the two first equations correspond to $\mathcal{S}\boldsymbol{u}_{so} = \mathcal{D}'\mathcal{M}p_{so}$. Next, we evaluate $\mathcal{S}\boldsymbol{u}_{so}$.

The numerical integration formula for one element E is

$$a_h(\boldsymbol{u},\boldsymbol{v})|_E = \sum_{k,l=0}^{1} A_{kl}^E (\boldsymbol{u}^T \boldsymbol{K}^{-1} \boldsymbol{v})_{kl}^E. \tag{22}$$

In (22), the vertices kl are indexed 00, 10, 11, and 01 in the counterclockwise direction from the lower left. The weight A_{kl}^E is one half of the area of the triangle in element E that contains the vertex kl; e.g., A_{00}^E is one half of the area of the triangle with vertices 00, 10, and 01, or equivalently, the area of the quadrilateral with corners at 00, at the midpoints of the two edges of E that meet at 00, and at the intersection of the two diagonals of E. A vector function $\boldsymbol{u}_{kl}^E$ at the vertex kl is described by its normal components $u\xi_k$ and $u\eta_l$ across the logically vertical and horizontal edges that meet at kl; because $\boldsymbol{RT}_0$ functions have constant normal components along the edges, such a function can equivalently be evaluated as a vector at the vertex or componentwise at the midpoints of the two side edges. We make the latter choice and consider the two edges as a local logical $\xi\eta$ coordinate system. The transform to the physical xy coordinate system can be described by

$$(\boldsymbol{u})_{\xi\eta} = \boldsymbol{G}(\boldsymbol{u})_{xy},$$

where $\boldsymbol{G}$ contains the unit vectors normal to the physical edges. That is,

$$(\boldsymbol{u})_{\xi\eta} = \begin{pmatrix} u\xi \\ u\eta \end{pmatrix} = \begin{pmatrix} (\boldsymbol{u})_{xy} \cdot \boldsymbol{n}_\xi \\ (\boldsymbol{u})_{xy} \cdot \boldsymbol{n}_\eta \end{pmatrix}.$$

In particular, in (22) this yields

$$(\boldsymbol{u}^T \boldsymbol{K}^{-1} \boldsymbol{v})_{xy} = \boldsymbol{u}_{\xi\eta}^T (\boldsymbol{G}^{-1})^T \boldsymbol{K}^{-1} \boldsymbol{G}^{-1} \boldsymbol{v}_{\xi\eta} = \boldsymbol{u}_{\xi\eta}^T \boldsymbol{T} \boldsymbol{v}_{\xi\eta}.$$

The transformation matrices $\boldsymbol{G}$ and $\boldsymbol{T}$ are described further in Appendix A. If we now use the numerical integration (22) with the Raviart-Thomas elements in equation (21) for one basis test function $\boldsymbol{v}_x \in \boldsymbol{V}_h$, associated to x-edge $(i-1/2, j)$,

$$\begin{aligned} a_h(\boldsymbol{u}_{so},\boldsymbol{v}_x) &= a_h(\boldsymbol{u}_{so},\boldsymbol{v}_x)|_{E_{i-1,j}} + a_h(\boldsymbol{u}_{so},\boldsymbol{v}_x)|_{E_{i,j}} \\ &= \sum_{m=0}^{1} \sum_{k,l=0}^{1} A_{kl}^{i-m,j} \begin{pmatrix} u\xi_k^{i-m,j} \\ u\eta_l^{i-m,j} \end{pmatrix}^T \boldsymbol{T}^{i-m,j} \begin{pmatrix} v\xi_k^{i-m,j} \\ v\eta_l^{i-m,j} \end{pmatrix} \\ &= \sum_{k,l=0}^{1} A_{kl}^{i-k,j} \begin{pmatrix} u\xi_k^{i-k,j} \\ u\eta_l^{i-k,j} \end{pmatrix}^T \boldsymbol{T}^{i-k,j} \begin{pmatrix} v\xi_k^{i-k,j} \\ 0 \end{pmatrix}. \end{aligned}$$

See Figure 3 for an illustration of the resulting flux molecule. Similarly,

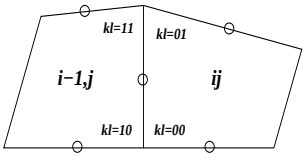

Figure 3. The resulting flux molecule for $a_h(\boldsymbol{u}_{so}, \boldsymbol{v}_x)$, when $\boldsymbol{v}_x$ has support in $E_{i,j}$ and $E_{i-1,j}$. This is equivalent to the first vector component of $(\mathcal{S}\boldsymbol{u})_{ij}$.

the numerical integration with basis test function $\boldsymbol{v}_y$ associated with y-edge $(i, j-1/2)$ becomes

$$a_h(\boldsymbol{u}_{so}, \boldsymbol{v}_y) = \sum_{k,l=0}^{1} A_{kl}^{i,j-l} \begin{pmatrix} u\xi_k^{i,j-l} \\ u\eta_l^{i,j-l} \end{pmatrix}^T \boldsymbol{T}^{i,j-l} \begin{pmatrix} 0 \\ v\eta_l^{i,j-l} \end{pmatrix}.$$

This completes the evaluation of $\mathcal{S}\boldsymbol{u}_{so}$.

As Figure 3 shows, the flux molecule for edge $(i-1/2, j)$ contains no other vertical edges such as $(i+1/2, j)$, unlike the MFEM and CVMFEM. This is due to the vertex-based numerical integration (22), which is akin to a trapezoidal rule. This suggests that the SOM is close to a MFEM or CVMFEM with a diagonalized ("lumped") mass matrix. It is not precisely that, however. The integration of Piola-transformed $\boldsymbol{RT}_0$ functions in MFEM or CVMFEM places the logical center of a quadrilateral at $F^E(1/2, 1/2)$, which is the intersection of the two segments that join the midpoints of opposite edges. For SOM, as noted above, the analogous point is the intersection of the two diagonals, which is different in general.

Next, the first vector component of $\mathcal{D}'\mathcal{M}\, p_{so}$ is equal to

$$\begin{aligned} (\operatorname{div} \boldsymbol{v}_x, p) &= p_{i-1,j} \int_{E_{i-1,j}} \operatorname{div} \boldsymbol{v}_x \, d\boldsymbol{x} + p_{ij} \int_{E_{ij}} \operatorname{div} \boldsymbol{v}_x \, d\boldsymbol{x} \\ &= p_{i-1,j} \left(\sum_{e \in E_{i-1,j}} \int_e \boldsymbol{v}_x \cdot \boldsymbol{n}_e \, ds \right) + p_{ij} \left(\sum_{e \in E_{ij}} \int_e \boldsymbol{v}_x \cdot \boldsymbol{n}_e \, ds \right) \\ &= (p_{i-1,j} - p_{i,j}) |h_{x_{ij}}|. \end{aligned}$$

The second component of $\mathcal{D}'\mathcal{M}\, p_{so}$ is similar in the j-direction. This development is analogous to the CVMFEM integration by parts in (18), and can be viewed as imposing weak continuity of the pressure in the context of SOM.

Finally, applying the discrete divergence operator $\mathcal{D}$ is equivalent to integrating the divergence of $\boldsymbol{u}$ multiplied by the test function $q =$

$\chi_E \in Q_h$ divided by the the area $|E_{ij}|$ of the element,

$$(\operatorname{div} \boldsymbol{u}, q_{ij}) = \int_{E_{ij}} \operatorname{div} \boldsymbol{u}\, d\boldsymbol{x} = \sum_{e \in E_{ij}} \int_e (\boldsymbol{u} \cdot \boldsymbol{n}_e) ds = (\mathcal{D}u)_{ij} |E|_{ij}.$$

The term G from equation (19) is equal to g_{ij}, which corresponds to (g, q_{ij}) approximated by $g_{ij}|E_{ij}|$ and then divided by $|E_{ij}|$.

6. The Expanded Mixed Finite Element Method

In [6] and [7] an expanded mixed finite element approximation, EMFEM, is discussed. The negative gradient of the pressure, $\tilde{\boldsymbol{u}} = -\operatorname{grad} p \in (\mathcal{L}^2)^2$, is introduced as a new variable. With the new variable equation (1) is now written as

$$\begin{aligned} \boldsymbol{u} &= \boldsymbol{K}(\boldsymbol{x})\tilde{\boldsymbol{u}} \\ \tilde{\boldsymbol{u}} &= -\operatorname{grad} p, \\ \operatorname{div} \boldsymbol{u} &= g. \end{aligned}$$

After writing the above equation in a weak form and approximating the continuous spaces, the EMFEM is: find $(\boldsymbol{u}_{ex}, \tilde{\boldsymbol{u}}_{ex}, p_{ex}) \in \boldsymbol{V}_h \times \tilde{\boldsymbol{V}}_h \times Q_h \subset H(\operatorname{div}) \times (\mathcal{L}^2)^2 \times \mathcal{L}^2$ such that

$$\begin{aligned} (\boldsymbol{u}_{ex}, \tilde{\boldsymbol{v}}) - (\boldsymbol{K}\tilde{\boldsymbol{u}}_{ex}, \tilde{\boldsymbol{v}}) &= 0 \qquad \text{for all } \tilde{\boldsymbol{v}} \in \tilde{\boldsymbol{V}}_h, \\ (\tilde{\boldsymbol{u}}_{ex}, \boldsymbol{v}) - (p_{ex}, \operatorname{div} \boldsymbol{v}) &= 0 \qquad \text{for all } \boldsymbol{v} \in \boldsymbol{V}_h, \\ (\operatorname{div} \boldsymbol{u}_{ex}, q) &= (g, q) \qquad \text{for all } q \in Q_h. \end{aligned} \tag{23}$$

The motivation for this formulation is its easier reducibility to a finite difference method that contains an explicit flux approximation involving $\boldsymbol{K}$. This is easier than in the MFEM because $\boldsymbol{K}$ appears directly in the equations. In the MFEM, the matrix representation of the $\boldsymbol{K}^{-1}$ term is sparse, with a full inverse matrix, and the flux approximation couples the entire grid unless a further reduction is made.

In [6] $\boldsymbol{K}$ is assumed smooth, and existence and uniqueness is proved for $(\boldsymbol{u}_{ex}, \tilde{\boldsymbol{u}}_{ex}, p_{ex})$. A superconvergence result is proved under certain conditions. Also, if $\tilde{\boldsymbol{u}}_{ex} \in \tilde{\boldsymbol{V}}_h$ implies that $\boldsymbol{K}\tilde{\boldsymbol{u}}_{ex} \in \tilde{\boldsymbol{V}}_h$ and if $\boldsymbol{V}_h \subset \tilde{\boldsymbol{V}}_h$, then the solution $(\boldsymbol{u}_{ex}, p_{ex})$ equals the MFEM solution $(\boldsymbol{u}_{mi}, p_{mi})$. To see this, let $\tilde{P}$ denote the $\mathcal{L}^2$-projection into $\tilde{\boldsymbol{V}}_h$; then from the first equation in (23), $\boldsymbol{u}_{ex} = \tilde{P}\boldsymbol{K}\tilde{\boldsymbol{u}}_{ex} = \boldsymbol{K}\tilde{\boldsymbol{u}}_{ex}$ pointwise, and $\boldsymbol{K}^{-1}\boldsymbol{u}_{ex} = \tilde{\boldsymbol{u}}_{ex}$ can again be used in the second equation in (23) to recover the classical MFEM. This implication typically holds in the case of an orthogonal

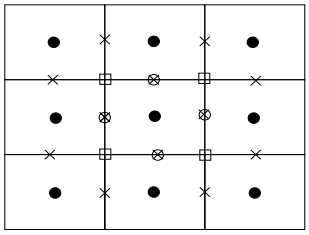

Figure 4. Computational molecule for CCFDM in the reference space, showing p (solid dots), $\boldsymbol{u}$ (open circles), $\tilde{\boldsymbol{u}}$ (crosses), and the evaluation of $\boldsymbol{K}$ (boxes at vertices).

grid with elementwise-constant diagonal permeability tensor. If the functions in $\tilde{\boldsymbol{V}}_h$ have continuous flux, then the implication requires $\boldsymbol{K}$ to be a global constant, not merely elementwise. This will be the situation in the next subsection.

6.1. Enhanced Cell-Centered Finite Difference Method

A cell-centered finite difference method, CCFDM, is the next step. The source for this method is the EMFEM from equation (23), with a specific choice of approximation spaces and numerical integration. $\boldsymbol{V}_h$ and Q_h are chosen to be the $\boldsymbol{RT}_0$ spaces from Section 3.2, $\tilde{\boldsymbol{V}}_h$ is chosen to be equal to $\boldsymbol{V}_h$, and numerical integration is as in [25] (trapezoidal rule in x and midpoint rule in y for the x-direction terms of vector integrals, the reverse for y-direction terms, and midpoint rule in both coordinates for scalar integrals). The advantages of this choice for $\tilde{\boldsymbol{V}}_h$ are an explicit flux expression with a nice computational molecule, consisting of nine points in 2D and 19 points in 3D, and a symmetric mass matrix. Before numerical integration, the grid is mapped to an orthogonal reference space. Let J denote the Jacobian and $\boldsymbol{D}$ the Jacobian matrix of this mapping. Letting $\boldsymbol{G} = \mathrm{J}\boldsymbol{D}^{-T}\boldsymbol{D}^{-1}$, [7] uses $\tilde{\boldsymbol{u}} = -\boldsymbol{G}^{-1}\operatorname{grad} p$, with test functions $\boldsymbol{G}\tilde{\boldsymbol{v}}$ instead of $\tilde{\boldsymbol{v}}$. This gives an analogue of the permeability,

$$\mathcal{K} = \mathrm{J}\boldsymbol{D}^{-1}\boldsymbol{K}\boldsymbol{D}^{-T}, \tag{24}$$

in the reference space. The resulting footprint of the CCFDM molecule is visualized in the reference space in Figure 4.

As long as $\mathcal{K}$ is continuous, the CCFDM performs well, and the choice of continuous-flux $\tilde{\boldsymbol{V}}_h = \boldsymbol{RT}_0$ does not cause a problem. However, for discontinuous $\mathcal{K}$, it is not possible to have a continuous normal component for both $\hat{\tilde{\boldsymbol{u}}}$ and $\hat{\boldsymbol{u}} = \mathcal{K}\hat{\tilde{\boldsymbol{u}}}$, where the hat marks the transformed quantities in the reference space. The effect of $\tilde{\boldsymbol{V}}_h = \boldsymbol{RT}_0$ on the accuracy of the method for discontinuous permeability can be illustrated in the case of an orthogonal grid and a diagonal permeability,

which is equivalent to the 1D situation in each direction. In 1D the permeability reduces to a scalar function k_i in cell i. Consider two neighboring cells i and $i+1$, with lengths h_i and h_{i+1} and permeabilities k_i and k_{i+1}, separated by edge $i+1/2$. The first two equations of (23) turn into

$$\begin{aligned}(h_i + h_{i+1})u_{i+1/2} &= (k_i h_i + k_{i+1}h_{i+1})\tilde{u}_{i+1/2},\\ \frac{1}{2}(h_i + h_{i+1})\tilde{u}_{i+1/2} &= -(p_{i+1} - p_i).\end{aligned}$$

Elimination of $\tilde{u}_{i+1/2}$ then yields, not the harmonic mean of the permeability, but rather

$$u_{i+1/2} = -\frac{h_i k_i + h_{i+1}k_{i+1}}{1/2(h_i + h_{i+1})^2}(p_{i+1} - p_i)$$

across the edge $i+1/2$. For the classical cell-centered FDM in 1D it is known that the order of convergence is reduced if the arithmetic mean is used instead of harmonic mean; see Samarskij [32].

The harmonic mean in 1D can be derived from assumptions of continuous velocity, continuous pressure, and a pointwise Darcy law ([33], p. 83). In this case, the "edge" between two cells is a point, and weak continuity of the pressure is the same as strong continuity. Thus, the CCFDM lacks the weak pressure continuity exhibited by MFEM, CVMFEM, and SOM. In the 2D CCFDM, this weak continuity is restored by incorporating Lagrange multipliers along the edges of all discontinuity lines. This partial hybridization of the method, analogous to the outline in Section 3.1, is called Enhanced Cell-Centered Finite Differences (ECCFDM), and can be found in [7]. To see the effect of this modification in a simplified setting, recall the 1D example, and instead of enforcing weak continuity of the pressure with Lagrange multipliers choose $\tilde{u} \in \boldsymbol{RT}_0^{-1}$. The superscript -1 denotes a discontinuous normal velocity component, producing twice as many basis functions. With the same numerical integration, the harmonic mean in 1D is recovered as follows. If $\tilde{u}^-_{i+1/2}$ and $\tilde{u}^+_{i+1/2}$ denote the discrete values in cell i and $i+1$, respectively, the two first equations of (23) now become

$$\begin{aligned}u_{i+1/2} &= k_i \tilde{u}^-_{i+1/2},\\ u_{i+1/2} &= k_{i+1}\tilde{u}^+_{i+1/2}, \quad \text{and}\\ \frac{h_i}{2}\tilde{u}^-_{i+1/2} + \frac{h_{i+1}}{2}\tilde{u}^+_{i+1/2} &= -(p_{i+1} - p_i),\end{aligned}$$

so that elimination of $\tilde{u}^-_{i+1/2}$ and $\tilde{u}^+_{i+1/2}$ yields

$$u_{i+1/2} = -\frac{2k_i k_{i+1}}{h_i k_i + h_{i+1}k_{i+1}}(p_{i+1} - p_i). \tag{25}$$

ENHANCED CELL-CENTERED FINITE DIFFERENCES 419

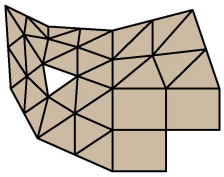

FIG. 10.3. *A complex domain with a hierarchical mesh.*

TABLE 10.1
The pressure error $\|P - p\|_{\mathrm{M}}$ *and the velocity error* $\|\mathbf{U} - \mathbf{u}\|_{\mathrm{M}}$ *for a hierarchical example.*

h	Mixed		Unenhanced cell-centered		Enhanced cell-centered	
	p	$\mathbf{u}$	p	$\mathbf{u}$	p	$\mathbf{u}$
0.16	0.39	6.0	0.48	9.3	0.59	6.4
0.08	0.11	3.1	0.12	5.9	0.11	3.5
0.04	0.029	1.5	0.043	3.7	0.026	1.6
0.02	0.0076	0.77	0.019	2.5	0.0062	0.80
Rate	h^2	h	$h^{1.4}$	$h^{0.6}$	h^2	h

Figure 5. Facsimile from [7] of an example demonstrating the need for Lagrange multipliers in light of convergence properties. Figure 10.3 shows the grid, and Table 10.1 compares the results from MFEM and the CCFDM with and without Lagrange multipliers. CCFDM with Lagrange multipliers is termed Enhanced cell-centered FDM (ECCFDM).

In a series of examples in [7], the authors show similarly that the convergence rate of the method is reduced if Lagrange multipliers are omitted. Figure 5 depicts a facsimile of one of the examples from [7].

From these examples, the prototypical 1D example, and the properties of the previously considered methods, the following hypothesis emerges.

OBSERVATION 1. *Weak continuity in the pressure is related to the rate of convergence across a discontinuity in the media.*

Weak continuity in the pressure in addition to flux continuity can be considered as a 2D or 3D analogue of the harmonic mean of the permeability in 1D. The other methods discussed in this paper will reduce to the FDM with harmonic mean in 1D, if the trapezoidal rule is used on the integrals.

If the Lagrange multipliers are to be avoided in the EMFEM, different approximation spaces are needed for $\tilde{\boldsymbol{u}}$ when $\boldsymbol{K}$ is discontinuous. The 1D example suggests using $\tilde{\boldsymbol{V}}_h = \boldsymbol{RT}_0^{-1}$ instead of $\boldsymbol{RT}_0$. Then the

EMFEM is: find $(\boldsymbol{u}_h, \tilde{\boldsymbol{u}}_h, p_h) \in \boldsymbol{RT}_0 \times \boldsymbol{RT}_0^{-1} \times Q_h$ such that

$$\begin{aligned} (\boldsymbol{u}_h, \tilde{\boldsymbol{v}}) - (\boldsymbol{K}\tilde{\boldsymbol{u}}_h, \tilde{\boldsymbol{v}}) &= 0 \qquad \text{for all } \tilde{\boldsymbol{v}} \in \boldsymbol{RT}_0^{-1}, \\ (\tilde{\boldsymbol{u}}_h, \boldsymbol{v}) - (p_h, \operatorname{div} \boldsymbol{v}) &= 0 \qquad \text{for all } \boldsymbol{v} \in \boldsymbol{RT}_0, \\ (\operatorname{div} \boldsymbol{u}_h, q) &= (g, q) \qquad \text{for all } q \in Q_h. \end{aligned} \tag{26}$$

Now the trapezoidal rule gives the harmonic mean on an orthogonal grid with diagonal $\boldsymbol{K}$. For an arbitrary elementwise-constant tensor $\boldsymbol{K}$ on an orthogonal grid, it is not possible to eliminate $\tilde{\boldsymbol{u}}_h$ and find a finite difference expression in $\boldsymbol{u}_h$ and p_h. One way to circumvent this problem is to split the flux equation for each edge into two equal parts, and then eliminate $\tilde{\boldsymbol{u}}$ for the four half-edges meeting at one cell vertex. To obtain the same number of unknowns as equations, the unknowns $\boldsymbol{u}_h$ and $\tilde{\boldsymbol{u}}_h$ must also be split for each edge. The resulting equation coincides with the multi-point flux-approximation (MPFA) O-method, derived along quite different lines in the next section. The underlying principle of MPFA is a control-volume method in which the flux approximation assumes continuous flux and a weaker continuity in the pressure. Thus, MPFA shares many of the important properties of the other MFEM-related methods.

7. The Multi-Point Flux Approximation Control Volume Method

Multi-point flux approximation (MPFA) uses more than two points in the flux approximation, as the name indicates, in a control-volume formulation. The MPFA methodology includes choices of parameters, and can be considered as a class of methods in the same way as the MFEM. MPFA methods are further described in [8, 9, 10, 11, 12, 13]. They are generalizations of the more classical finite volume or control volume method, in which two points approximate the flux, using the harmonic mean of discontinuous permeabilities as in the last section. Continuity of the pressure and the flux underlies both the harmonic mean and the generalizations to MPFA.

The classical finite volume method reads:

$$\begin{aligned} \sum_{e \in E} f_e &= \int_E g \, d\boldsymbol{x} \qquad \text{for all } \ E \in \mathcal{T}_h, \\ f_e &= t_e(p_{e^-} - p_{e^+}) \qquad \text{for all } \ e \in \mathcal{E}_h. \end{aligned}$$

The coefficient t_e is often called the **transmissibility** for the edge e, and $p_{e^\pm}$ are the pressures in the cells on either side of the edge. The pressure in cell k is associated with a grid point $\boldsymbol{x}_k$, preferably the

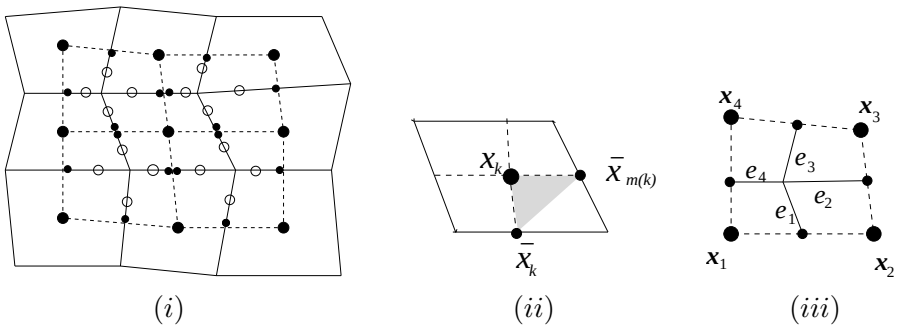

Figure 6. (*i*) Computational molecule for MPFA, showing nine grid cells (solid lines; large cell-centered dots denote cell pressures) and four interaction regions (dashed lines). Edge pressures (smaller filled dots) are eliminated to obtain transmissibilities. Fluxes (open circles) are calculated for each sub-edge (half-edge). (*ii*) One grid cell, divided into four sub-cells. Grid-point and edge-point labels are for lower-right (shaded) interaction region; $m(k) = k - 1$ unless $k = 1$, $m(1) = 4$. (*iii*) One interaction region.

centroid. To begin the generalization to MPFA, choose an edge point $\bar{\boldsymbol{x}}_i$ for each cell edge i. Around each vertex, draw a closed polygon joining the grid points $\boldsymbol{x}_k$ and the edge points $\bar{\boldsymbol{x}}_i$; this defines the **interaction regions**. Each edge point divides its edge into two parts, called **sub-edges**; similarly each cell is divided into four **sub-cells**. Figure 6 illustrates the details, as in [11]. If instead one edge point is chosen for each sub-edge, i.e., two edge points for each edge, the method of [12] is obtained.

The MPFA *O*-method will be described here. The flux over a sub-edge is approximated by a weighted sum of the pressures at the four grid points in an interaction region:

$$f_i = \sum_{k=1}^{4} t_k p_k \qquad \text{for the sub-edge } i, \tag{27}$$

where counterclockwise is taken to be the positive flux direction. The interaction region is used to determine the transmissibilities t_k locally. Details of the derivation of the transmissibility coefficients are given in [8], and we summarize them here. Allow the pressure to be a linear (not bilinear) function in each of the four sub-cells of the interaction region, for a total of 12 degrees of freedom. In each sub-cell, the three pressures at the grid point and the two edge points determine the pressure function, and by Darcy's law they also determine the flux (a constant vector on each sub-cell). The degrees of freedom are not sufficient to obtain continuity in both the pressure and the flux, so that weaker continuity is imposed on the discrete pressure. The 12 constraints are

the pressures at the four grid points, pressure continuity at the four edge points (this choice motivates the name of the O-method, because of the shape of the polylines connecting the grid points in the flux molecule), and flux continuity at the four sub-edges.

With cellwise constant permeability, the linear pressure yields a constant normal flux component on each sub-edge, so that the flux is continuous pointwise, as in the MFEM, CVMFEM, SOM, and EC-CFDM. In general, the weak continuity of p is not equivalent to that of the other methods. If two edge points are chosen on each edge, at the midpoint of each sub-edge [12] [13], then we have $\int_{e_i}[p]ds = 0$ on each edge due to linearity and continuity at the midpoint. This is analogous to the situation with MFEM and the other methods, but applied to sub-edges instead of edges. In the MPFA O-method under consideration here, the edge point is at one end of the sub-edge, so that $\int_{e_i}[p]ds = 0$ need not hold.

To complete the description of MPFA, we will now give more details of the transmissibility derivation. The flux through each sub-edge is found from the assumptions of Darcy's law and linear pressure in each sub-cell of the interaction region. Denote these sub-cells by $k = 1, \ldots, 4$, and similarly denote the local sub-edges in the interaction region $i = 1, \ldots, 4$, as in Figure 6-(iii). Proceeding counterclockwise in the figure, denote the edge point preceding grid point $\boldsymbol{x}_k$ by $\bar{\boldsymbol{x}}_{m(k)}$; see Figure 6-($ii$). Then $m(k) = k - 1$ unless $k = 1$, and $m(1) = 4$. Henceforth, for convenience, ignore the exception in the notation, and write $\bar{\boldsymbol{x}}_k$ and $\bar{\boldsymbol{x}}_{k-1}$ for the edge points of sub-cell k. Let $\boldsymbol{n}_i$ be a unit normal vector on sub-edge i, pointing out of sub-cell i (counterclockwise in Figure 6-(iii)). Let f_{ik} be the flux through sub-edge i, out of sub-cell k if $i = k$, and into sub-cell k if $i = k - 1$. Then Darcy's law yields

$$f_{ik} = -\boldsymbol{n}_i^T \boldsymbol{K}^k \operatorname{grad}(p)|e_i|. \tag{28}$$

The next step is to determine $\operatorname{grad}(p)$ from the linear pressure variation between the grid point $\boldsymbol{x}_k$ and the two edge points $\bar{\boldsymbol{x}}_k$ and $\bar{\boldsymbol{x}}_{k-1}$ of sub-cell k; see Figure 6-(ii). Details can be found in [11], p. 410.

For each sub-cell k

$$\begin{aligned} \operatorname{grad}(p) \cdot (\bar{\boldsymbol{x}}_k - \boldsymbol{x}_k) &= \bar{p}_k - p_k, \\ \operatorname{grad}(p) \cdot (\bar{\boldsymbol{x}}_{k-1} - \boldsymbol{x}_k) &= \bar{p}_{k-1} - p_k, \end{aligned} \tag{29}$$

where $\bar{p}_k = p(\bar{\boldsymbol{x}}_k)$, $p_k = p(\boldsymbol{x}_k)$. From this expression the discrete gradient on sub-cell k can be written as

$$\operatorname{grad}(p) = \frac{1}{T_k} \sum_{l=0}^{1} (\bar{\boldsymbol{x}}_{k-1+l} - \boldsymbol{x}_k)^{\perp} (\bar{p}_{k-l} - p_k), \tag{30}$$

where T_k is equal to twice the area of the triangle spanned by the points $\boldsymbol{x}_k$, $\bar{\boldsymbol{x}}_k$ and $\bar{\boldsymbol{x}}_{k-1}$, and the vectors $(\bar{\boldsymbol{x}}_{k-l}-\boldsymbol{x}_k)^\perp$, $l = 0, 1$, have the lengths of $\bar{\boldsymbol{x}}_{k-l} - \boldsymbol{x}_k$ and point into the interaction region. Incorporating the gradient expression (30) in the flux expression (28) gives

$$f_{ik} = \sum_{l=0}^{1} \omega_{ikl}(\bar{p}_{k-l} - p_k), \tag{31}$$

where

$$\omega_{ikl} = -\frac{\boldsymbol{n}_i^T \boldsymbol{K}^k}{T_k}(\bar{\boldsymbol{x}}_{k-1+l} - \boldsymbol{x}_k)^\perp |e_i|.$$

In each interaction region we get eight equations like (31), from the two sub-edges of each of the four sub-cells of the interaction region. Define the vectors

$$\begin{aligned}
\boldsymbol{p} &= [p_1, \ldots, p_4]^T, \\
\bar{\boldsymbol{p}} &= [\bar{p}_1, \ldots, \bar{p}_4]^T, \\
\boldsymbol{f}_1 &= [f_{11}, f_{22}, f_{33}, f_{44}]^T, \quad \text{and} \\
\boldsymbol{f}_2 &= [f_{12}, f_{23}, f_{34}, f_{41}]^T.
\end{aligned}$$

The eight equations from (31) can then be written in matrix form as,

$$\boldsymbol{f}_1 = \boldsymbol{A}\bar{\boldsymbol{p}} + \boldsymbol{B}\boldsymbol{p}, \tag{32}$$

$$\boldsymbol{f}_2 = \boldsymbol{C}\bar{\boldsymbol{p}} + \boldsymbol{D}\boldsymbol{p}. \tag{33}$$

The matrix is written out in Appendix B. The flux continuity condition at each of the four sub-edges gives $\boldsymbol{f}_1 = \boldsymbol{f}_2$, that is,

$$\boldsymbol{A}\bar{\boldsymbol{p}} + \boldsymbol{B}\boldsymbol{p} = \boldsymbol{C}\bar{\boldsymbol{p}} + \boldsymbol{D}\boldsymbol{p},$$

or

$$\bar{\boldsymbol{p}} = (\boldsymbol{A} - \boldsymbol{C})^{-1}(\boldsymbol{D} - \boldsymbol{B})\boldsymbol{p}. \tag{34}$$

Eliminating $\bar{\boldsymbol{p}}$ in (32) via (34) gives the transmissibility matrix $\boldsymbol{T}$ as follows for $\boldsymbol{f} = \boldsymbol{f}_1$:

$$\boldsymbol{f} = \boldsymbol{T}\,\boldsymbol{p} = \Big(\boldsymbol{A}(\boldsymbol{A} - \boldsymbol{C})^{-1}(\boldsymbol{D} - \boldsymbol{B}) + \boldsymbol{B}\Big)\,\boldsymbol{p}. \tag{35}$$

The rows in $\boldsymbol{T}$ contain the coefficients associated with the sub-edges 1 to 4, respectively. This expression is generally not possible to describe in a simpler way, and usually becomes rather complicated.

7.1. Multi-Point Flux Approximation and the Expanded Mixed Finite Element Method

In this section we consider rectangular grids. The permeability is still assumed to be an elementwise constant full tensor. We will show the connection between MPFA and EMFEM, by first writing EMFEM with numerical integration as a set of discrete equations, and then rewriting the corresponding set of MPFA equations in a similar way by introducing a discrete-gradient variable. Theorem 1 shows that amalgamation of the MPFA solution yields the EMFEM solution. Thus, on rectangular grids, the MPFA results immediately give the EMFEM results, but not conversely, and the amalgamation of the MPFA has the same weak continuity property as the EMFEM.

Recall the EMFEM with different approximation spaces for the velocity and the new variable, $\tilde{\boldsymbol{u}} = -\operatorname{grad} p$, as given in (26). The finite difference formulation is found from (26) when trapezoidal numerical integration (as for (23) in Section 6.1) is used on the terms $(\tilde{\boldsymbol{u}}_h, \boldsymbol{v})$, $(\boldsymbol{u}_h, \tilde{\boldsymbol{v}})$, and $(\boldsymbol{K}\tilde{\boldsymbol{u}}_h, \tilde{\boldsymbol{v}})$. Let $(\ \cdot, \cdot\ )_T$ denote that the trapezoidal rule is applied. With this notation the new finite difference system can be written as: find $(\boldsymbol{u}_h, \tilde{\boldsymbol{u}}_h, p_h) \in \boldsymbol{RT}_0 \times \boldsymbol{RT}_0^{-1} \times Q_h$ such that

$$\begin{aligned} (\boldsymbol{u}_h, \tilde{\boldsymbol{v}})_T - (\boldsymbol{K}\tilde{\boldsymbol{u}}_h, \tilde{\boldsymbol{v}})_T &= 0, && \text{for all } \tilde{\boldsymbol{v}} \in \boldsymbol{RT}_0^{-1}, \\ (\tilde{\boldsymbol{u}}_h, \boldsymbol{v})_T - (p_h, \operatorname{div} \boldsymbol{v}) &= 0, && \text{for all } \boldsymbol{v} \in \boldsymbol{RT}_0, \\ (\operatorname{div} \boldsymbol{u}_h, q) &= (g, q), && \text{for all } q \in Q_h. \end{aligned} \tag{36}$$

Let $\boldsymbol{v}_{i\pm1/2,j}$ and $\boldsymbol{v}_{i,j\pm1/2}$ denote the basis functions of $\boldsymbol{RT}_0$ associated with the edges $(i \pm 1/2, j)$ and $(i, j \pm 1/2)$, scaled such that $\boldsymbol{v}_e \cdot \boldsymbol{n}_e = 1$ for the edge e with a unit normal vector $\boldsymbol{n}_e$. Similarly let the basis functions of $\boldsymbol{RT}_0^{-1}$ be denoted $\tilde{\boldsymbol{v}}^{\pm}_{i\pm1/2,j}$ and $\tilde{\boldsymbol{v}}^{\pm}_{i,j\pm1/2}$, since we do not have any continuity restrictions across the edges, and have two basis functions associated with each edge. Let $|\mathcal{T}|$ denote the number of elements in $\mathcal{T}_h$, and $|\mathcal{E}|$ the number of edges in $\mathcal{E}_h$. We will still use the MPFA terminology, where the two parts of a cell edge are sub-edges, and interaction regions form the dual grid. The two sides of a cell edge will be marked with superscript $-$ or $+$; see Figure 7-(i). Let generally $\{\boldsymbol{v}_e\}$ be the basis functions of $\boldsymbol{V}_h$, $\{\tilde{\boldsymbol{v}}_e^{\pm}\}$ the basis functions of $\tilde{\boldsymbol{V}}_h$, and $\{q_E\}$ the basis functions of Q_h. The discrete solution of (36) can then be termed $\{u_e, \tilde{u}_e, p_E\}_{E\in\mathcal{T}_h, e\in\mathcal{E}_h}$ with $\boldsymbol{u}_h = \sum u_e \boldsymbol{v}_e$, $\tilde{\boldsymbol{u}}_h = \sum \tilde{u}_e^{\pm} \tilde{\boldsymbol{v}}_e^{\pm}$, and $p_h = \sum p_E q_E$. If the integrations in (36) are written out with the test

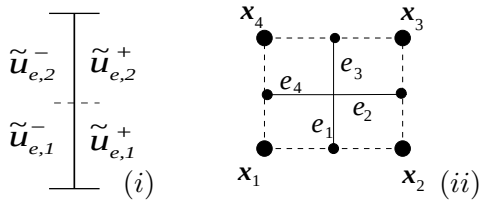

Figure 7. (*i*) One edge e with the four discrete gradient variables $\tilde{u}^{\pm}_{e,k}$. (*ii*) Interaction region.

functions $(\boldsymbol{v}_{i+1/2,j}, \tilde{\boldsymbol{v}}^{\pm}_{i+1/2,j}, q_{i,j})$, the EMFEM from (36) takes the form

$$u_{i+1/2,j} = k_x^{i,j}\tilde{u}^-_{i+1/2,j} + \frac{k_{xy}^{i,j}}{2}\tilde{u}^-_{i,j+1/2} + \frac{k_{xy}^{i,j}}{2}\tilde{u}^+_{i,j-1/2},$$

$$u_{i+1/2,j} = k_x^{i+1,j}\tilde{u}^+_{i+1/2,j} + \frac{k_{xy}^{i+1,j}}{2}\tilde{u}^-_{i+1,j+1/2} + \frac{k_{xy}^{i+1,j}}{2}\tilde{u}^+_{i+1,j-1/2}, \quad (37)$$

$$\frac{h_i}{2}\tilde{u}^-_{i+1/2,j} + \frac{h_{i+1}}{2}\tilde{u}^+_{i+1/2,j} = -(p_{i+1,j} - p_{i,j}), \quad (38)$$

$$\sum_{e\in\mathcal{E}_h\cap E_{ij}} \pm|e|u_e = (g, q_{i,j}), \quad (39)$$

where the plus sign holds in (39) if and only if $\boldsymbol{n}_e$ points into E_{ij}. The unknowns of interest are actually still $\boldsymbol{u}_h$ and p_h, while $\tilde{\boldsymbol{u}}_h$ can be considered as an intermediate quantity. We then get $2|\mathcal{E}|$ discrete unknowns of $\tilde{\boldsymbol{u}}_h$, $|\mathcal{E}|$ unknowns of $\boldsymbol{u}_h$, and $|\mathcal{T}|$ unknowns of p_h, and we have $2|\mathcal{E}|$ equations of type (37), $|\mathcal{E}|$ equations of type (38), and $|\mathcal{T}|$ equations of type (39).

We now seek to rewrite the MPFA system from the previous section in an expanded form similar to the EMFEM system (37)-(39). Define the discrete MPFA velocity (sub-edge flux divided by sub-edge length) for each sub-edge of edge e as $u_{e,1}$ for the lower or left sub-edge, and $u_{e,2}$ for the upper or right sub-edge. Similarly define the discrete MPFA gradients (actually, scalar normal components of gradients) as four unknowns for each edge; see Figure 7-(*i*) for an illustration on edge $e = (i + 1/2, j)$. Consider sub-cell 1 in Figure 7-(*ii*), connected to sub-edges e_1 and e_4. From the MPFA assumption of linear pressure variation in each sub-cell, the gradient is constant. The discrete MPFA gradient values for each sub-edge can then be used in the gradient expression such that

$$-\operatorname{grad}(p) = \begin{pmatrix} \tilde{u}^-_{e_1} \\ \tilde{u}^-_{e_4} \end{pmatrix}. \quad (40)$$

Now calculating the flux from Darcy's law, as in (28), from sub-cell 1 across sub-edge e_1,

$$f_{11} = -\boldsymbol{K}^1 \operatorname{grad}(p) \cdot \begin{pmatrix} 1 \\ 0 \end{pmatrix} |e_1| = (k_x^1 \tilde{u}_{e_1}^- + k_{xy}^1 \tilde{u}_{e_4}^-)|e_1|, \tag{41}$$

corresponding to the discrete velocity

$$u_{e_1} = k_x^1 \tilde{u}_{e_1}^- + k_{xy}^1 \tilde{u}_{e_4}^-. \tag{42}$$

If sub-edge e_1 is the upper sub-edge of edge $(i+1/2, j)$, then this yields

$$u_{i+1/2,j,2} = k_x^{i,j} \tilde{u}_{i+1/2,j,2}^- + k_{xy}^{i,j} \tilde{u}_{i,j+1/2,2}^-. \tag{43}$$

An analogous derivation for sub-cell 2 and sub-edge e_1 gives

$$f_{12} = -\boldsymbol{K}^2 \operatorname{grad}(p) \cdot \begin{pmatrix} 1 \\ 0 \end{pmatrix} |e_1| = (k_x^2 \tilde{u}_{e_1}^+ + k_{xy}^2 \tilde{u}_{e_2}^-)|e_1|,$$

hence

$$u_{i+1/2,j,2} = k_x^{i+1,j} \tilde{u}_{i+1/2,j,2}^+ + k_{xy}^{i+1,j} \tilde{u}_{i+1,j+1/2,1}^-. \tag{44}$$

With sub-cells 4 and 3 and sub-edge e_3, if e_3 is the lower sub-edge of edge $(i+1/2, j)$, we get

$$u_{i+1/2,j,1} = k_x^{i,j} \tilde{u}_{i+1/2,j,1}^- + k_{xy}^{i,j} \tilde{u}_{i,j-1/2,2}^+, \tag{45}$$

$$u_{i+1/2,j,1} = k_x^{i+1,j} \tilde{u}_{i+1/2,j,1}^+ + k_{xy}^{i+1,j} \tilde{u}_{i+1,j-1/2,1}^+. \tag{46}$$

Note the similarity between the first equation (37) and the sum of (43) and (45), and analogously for the second equation (37) and the sum of (44) and (46). Next, let h_1 and h_2 be the lengths of cells 1 and 2 in the x-direction. Now using the gradient expression (40) directly in (29) for sub-cells 1 and 2 connected by sub-edge e_1 gives

$$-\tilde{u}_{e_1}^- \frac{h_1}{2} = \bar{p}_1 - p_1 \qquad \text{and} \qquad \tilde{u}_{e_1}^+ \frac{h_2}{2} = \bar{p}_1 - p_2.$$

Eliminating $\bar{p}_1$ as in the original derivation of MPFA, equation (34) to (35), gives

$$\frac{h_1}{2} \tilde{u}_{e_1}^- + \frac{h_2}{2} \tilde{u}_{e_1}^+ = -(p_2 - p_1).$$

If e_1 is the upper sub-edge of edge $(i+1/2, j)$, this yields

$$\frac{h_i}{2} \tilde{u}_{i+1/2,j,2}^- + \frac{h_{i+1}}{2} \tilde{u}_{i+1/2,j,2}^+ = -(p_{i+1,j} - p_{i,j}). \tag{47}$$

Analogously, from sub-edge e_3 and sub-cells 4 and 3,

$$\frac{h_i}{2} \tilde{u}_{i+1/2,j,1}^- + \frac{h_{i+1}}{2} \tilde{u}_{i+1/2,j,1}^+ = -(p_{i+1,j} - p_{i,j}). \tag{48}$$

The average of (47) and (48) is similar to (38). Finally, we have the cell conservation equations

$$\sum_{e\in\mathcal{E}_h\cap E_{ij}} \pm|e|(u_{e,1}+u_{e,2})/2 = (g,q_{i,j}), \tag{49}$$

with signs as in (39). We have $4|\mathcal{E}|$ unknowns of $\tilde{\boldsymbol{u}}$, $2|\mathcal{E}|$ unknowns of $\boldsymbol{u}$, and $|\mathcal{T}|$ unknowns of p, and we have $4|\mathcal{E}|$ equations of type (43)-(46), $2|\mathcal{E}|$ equations of type (47)-(48), and $|\mathcal{T}|$ equations of type (49). Introduce the index $\xi = 0, 1$, associate the superscript $-$ with $\xi = 0$, and the superscript $+$ with $\xi = 1$. The MPFA method can then be rewritten in expanded form as: $\{u_{e,k}, \tilde{u}^{\pm}_{e,k}, p^E\}_{E\in\mathcal{T}_h, e\in\mathcal{E}_h, k\in\{1,2\}, \xi\in\{0,1\}}$ such that

$$\begin{aligned}
&u_{i+1/2,j,k} = k_x^{i+\xi,j}\tilde{u}^{\xi}_{i+1/2,j,k} + k_{xy}^{i+\xi,j}\tilde{u}^{2-k}_{i+\xi,j-3/2+k,2-\xi}, && (i+1/2,j)\in\mathcal{E}_h,\\
&u_{i,j+1/2,k} = k_y^{i,j+\xi}\tilde{u}^{\xi}_{i,j+1/2,k} + k_{xy}^{i,j+\xi}\tilde{u}^{2-k}_{i-3/2+k,j+\xi,2-\xi}, && (i,j+1/2)\in\mathcal{E}_h,\\
& && k=1,2, \quad \xi=0,1,\\
&\frac{h_i}{2}\tilde{u}^{-}_{i+1/2,j,k} + \frac{h_{i+1}}{2}\tilde{u}^{+}_{i+1/2,j,k} = -(p_{i+1,j}-p_{i,j}), && (i+1/2,j)\in\mathcal{E}_h,\\
&\frac{h_j}{2}\tilde{u}^{-}_{i,j+1/2,k} + \frac{h_{j+1}}{2}\tilde{u}^{+}_{i,j+1/2,k} = -(p_{i,j+1}-p_{i,j}), && (i,j+1/2)\in\mathcal{E}_h,\\
& && k=1,2,\\
&\sum_{e\in\mathcal{E}_h\cap E_{ij}} |e|(u_{e,1}+u_{e,2})/2 = (g,q_{i,j}), && E_{ij}\in\mathcal{T}_h.
\end{aligned} \tag{50}$$

A proof of existence and uniqueness for the MPFA solution ($\boldsymbol{u}$ and p) in case of rectangular grids can be found in [10]. To show that there is also a unique gradient $\tilde{\boldsymbol{u}}$ for the expanded form, note that for each corner in each cell we can derive a local connection between the $\tilde{\boldsymbol{u}}$- and $\boldsymbol{u}$-solution. Let the edges e_1 and e_2 meet in the upper right-hand corner of a cell E; see Figure 8. Define $\boldsymbol{U}_c = [u_{e_1,2}, u_{e_2,2}]^T$ and $\tilde{\boldsymbol{U}}_c = [\tilde{u}^-_{e_1,2}, \tilde{u}^-_{e_2,2}]^T$; then $\boldsymbol{U}_c = \boldsymbol{K}^E\tilde{\boldsymbol{U}}_c$, from the first two equations of (50) with $k=2$ and $\xi=0$, hence $\tilde{\boldsymbol{U}}_c = (\boldsymbol{K}^E)^{-1}\boldsymbol{U}_c$.

It remains to prove the relationship between the EMFEM from (36) and the expanded MPFA method from (50).

THEOREM 1. *Let $\{u_{e,k}, \tilde{u}^{\pm}_{e,k}, p_{E,mp}\}_{e\in\mathcal{E}_h, E\in\mathcal{T}_h}$ be the MPFA solution of (50), and let the EMFEM solution of (36) be $\{u_e, \tilde{u}^{\pm}_e, p_{E,em}\}_{e\in\mathcal{E}_h, E\in\mathcal{T}_h}$. For each element, E, define the local element edges e_1 to e_4, and the sub-edges $e_i,1$ and $e_i,2$, as in Figure 8. Let*

$$\begin{aligned}
\boldsymbol{V}^E &= [u_{e_1},\ldots,u_{e_4}]^T, \text{ and}\\
\boldsymbol{U}^E &= [u_{e_1,2}, u_{e_1,1}, \ldots, u_{e_4,2}, u_{e_4,1}]^T.
\end{aligned}$$

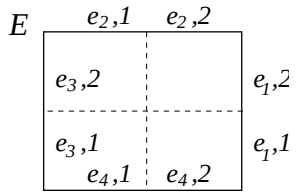

Figure 8. An element, E, the local edges, e_1 to e_4, and the sub-edges e_ik, for $i = 1, \ldots, 4$, and $k = 1, 2$.

Then

$$\begin{aligned} \boldsymbol{V}^E &= \boldsymbol{Q}^E \boldsymbol{U}^E, && \textit{for all } E \in \mathcal{T}_h, \\ \tilde{u}_e^{\pm} &= (\tilde{u}_{e,1}^{\pm} + \tilde{u}_{e,2}^{\pm})/2, && \textit{for all } e \in \mathcal{E}_h, \\ p_{E,em} &= p_{E,mp}, && \textit{for all } E \in \mathcal{T}_h, \end{aligned} \tag{51}$$

where

$$\boldsymbol{Q}^E = \frac{1}{4} \begin{bmatrix} \alpha & \alpha & -\beta & \beta & \delta & \delta & -\beta & \beta \\ -\gamma & \gamma & \alpha & \alpha & -\gamma & \gamma & \delta & \delta \\ \delta & \delta & \beta & -\beta & \alpha & \alpha & \beta & -\beta \\ \gamma & -\gamma & \delta & \delta & \gamma & -\gamma & \alpha & \alpha \end{bmatrix}, \tag{52}$$

with

$$\alpha = \frac{2\, k_x^E\, k_y^E - (k_{xy}^E)^2}{k_x^E\, k_y^E - (k_{xy}^E)^2}, \quad \beta = \frac{k_x^E\, k_{xy}^E}{k_x^E\, k_y^E - (k_{xy}^E)^2},$$
$$\gamma = \frac{k_{xy}^E\, k_y^E}{k_x^E\, k_y^E - (k_{xy}^E)^2}, \quad \textit{and} \quad \delta = -\frac{(k_{xy}^E)^2}{k_x^E\, k_y^E - (k_{xy}^E)^2}.$$

Proof. Under the connection given above we will show that the expanded MPFA set of equations equals the EMFEM equations. The calculations will be done for a general element E_{ij}, and a general edge $e = (i+1/2, j)$, such that the expanded MPFA is described by (43)-(49), while (37)-(39) represent the EMFEM. First observe that equations (47) and (48) sum to equation (38) under the relationship

$$\tilde{u}_{i+1/2,j}^{\pm} = (\tilde{u}_{i+1/2,j,1}^{\pm} + \tilde{u}_{i+1/2,j,2}^{\pm})/2. \tag{53}$$

Then observe that the rest of the equations can be studied on each element separately. On element E, define $\boldsymbol{V}$ and $\boldsymbol{U}$ as $\boldsymbol{V}^E$ and $\boldsymbol{U}^E$ above, and

$$\tilde{\boldsymbol{V}} = [\tilde{u}_{e_1}^-, \tilde{u}_{e_2}^-, \tilde{u}_{e_3}^+, \tilde{u}_{e_4}^+]^T, \tag{54}$$
$$\tilde{\boldsymbol{U}} = [\tilde{u}_{e_1,2}^-, \tilde{u}_{e_1,1}^-, \ldots, \tilde{u}_{e_4,2}^+, \tilde{u}_{e_4,1}^+]^T \tag{55}$$

from the EMFEM and expanded MPFA, respectively. We have dropped the superscript E for simplicity. For EMFEM this means that the

analogue of equation (37) on one element can be described by a 4×4 matrix as

$$\boldsymbol{V} = \boldsymbol{M}\tilde{\boldsymbol{V}}.$$

The matrix $\boldsymbol{M}$ is detailed in Appendix B, equation (68). Similarly we can define an 8×8 matrix, $\boldsymbol{N}$, from the analogues of equations (43)–(46) such that

$$\boldsymbol{U} = \boldsymbol{N}\tilde{\boldsymbol{U}}.$$

The matrix $\boldsymbol{N}$ appears in Appendix B, equation (69). The connection in equation (53) related to element E becomes

$$\tilde{\boldsymbol{V}} = \boldsymbol{P}\tilde{\boldsymbol{U}},$$

where $\boldsymbol{P}$ is a 4×8 matrix in Appendix B. The connection between $\boldsymbol{V}$ and $\boldsymbol{U}$ is then given by

$$\boldsymbol{V} = \boldsymbol{M}\boldsymbol{P}\boldsymbol{N}^{-1}\boldsymbol{U} \equiv \boldsymbol{Q}^E\boldsymbol{U}, \tag{56}$$

where $\boldsymbol{Q}^E$ is a 4×8 matrix. The column sums of $\boldsymbol{Q}^E$ equal $1/2$ in such a way that the connection (56) gives equation (49) from equation (39). □

Even if MPFA does not have weak continuity in the Lagrange-multiplier sense on each sub-edge, it can be considered to have this property on each edge through the local operator $\boldsymbol{Q}^E$, and the connections to the EMFEM.

Also note that symmetry for MPFA on orthogonal grids follows directly from equation (50). The discrete EMFEM set of equations (37)-(39) is symmetric before common multiplicative factors are dropped: multiply the two equations of (37) by $h_i h_j/2$ and $h_{i+1}h_j/2$, respectively, and equation (38) by h_j, and the symmetry follows. Similarly for the MPFA set of equations in (50), multiply the first four equations by $h_{i+\xi}h_j/2$, $h_i h_{j+\xi}/2$, h_j, and h_i, respectively, and again the symmetry follows. The MPFA set of equations from (50) can then be written in matrix form as

$$\begin{pmatrix} \boldsymbol{A} & \boldsymbol{B}^T & 0 \\ \boldsymbol{B} & 0 & \boldsymbol{C}^T \\ 0 & \boldsymbol{C} & 0 \end{pmatrix} \begin{pmatrix} \tilde{U} \\ U \\ P \end{pmatrix} = \begin{pmatrix} 0 \\ 0 \\ Q \end{pmatrix}.$$

After elimination of the discrete gradients $\tilde{U}$ and velocities U, the system for the discrete pressures P, $\boldsymbol{C}(\boldsymbol{B}\boldsymbol{A}^{-1}\boldsymbol{B}^T)^{-1}\boldsymbol{C}^T P = Q$, is still symmetric. Symmetry for MPFA on orthogonal grids in 3D is shown in [10] with a rather lengthy proof.

Symmetry as derived above for rectangular grids does not extend to general quadrilaterals, since $\bar{\boldsymbol{x}}_k - \boldsymbol{x}_k$ from equation (29) in this case does not correspond to the cell edge used in equation (41); see Figure 6-(*ii*). However, for a version of MPFA derived from an orthogonal reference space, the connection to the EMFEM does extend to general quadrilateral grids (see [35]), and symmetry extends as well.

8. Numerical Experiment

The methods discussed here are all described in a number of publications along with numerical tests to verify their favorable qualities. To a certain extent the numerical experiments described in the literature discuss the same cases. All the methods are tested with distorted irregular grids and layered media, including the case with uniform flow where all the methods reproduce the exact solution except for the MPFA version discussed in [13]. Numerical experiments with the CVMFEM are performed in [14] and [3]. For the SOM a good source of information on numerical experiments is [5]. In [6] and [7] the EMFEM and the derived ECCFDM are developed and tested. Solutions for discontinuities in the media are discussed in section 6.1 of this paper. Experimental analysis of the MPFA O-method convergence is done in [34]. Numerical tests are also performed in [13] for the MPFA version described there.

One new, simple, non-orthogonal example here will illustrate good convergence qualities of the considered methods. The grid is built on parallelograms which still give affine elements, except along the boundary. The grid and the refinement strategy are shown in Figure 9. The

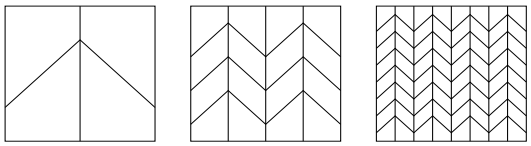

Figure 9. Refinement of the grid

permeability is chosen to be homogeneous. Except for the boundary elements, this corresponds in a reference space to an elementwise constant permeability on an orthogonal grid. Since the grid mainly consists of two types of parallelograms, the transformed permeability $\mathcal{K}$ from (24) will vary between

$$\mathcal{K}_1 = \begin{pmatrix} 2 & 1 \\ 1 & 1 \end{pmatrix} \qquad \text{and} \qquad \mathcal{K}_2 = \begin{pmatrix} 2 & -1 \\ -1 & 1 \end{pmatrix},$$

except along the boundary. This is a rather small discontinuity. The boundary condition is chosen such that the exact solution is

$$p(x,y) = \cosh(\pi x)\cos(\pi y) \quad \text{on} \quad [0,1]\times[0,1].$$

The numerical error is measured in the following discrete $\mathcal{L}^2$ norms:

$$ep = \left(\sum_{ij\in\mathcal{T}_h} A_{ij}(p_{ij} - p(\boldsymbol{x}_{ij})^2) \Big/ \sum_{ij\in\mathcal{T}_h} A_{ij} \right)^{1/2}, \tag{57}$$

$$ev = \left(\sum_{e\in\mathcal{E}_h} Q_e(f_e - f_e/|e|))^2 \Big/ \sum_{e\in\mathcal{E}_h} Q_e \right)^{1/2}. \tag{58}$$

Here A_{ij} is the area of element ij, while Q_e is the area associated with edge e, illustrated in Figure 2 for the edge $e = (i+1/2, j)$. Numerical results are shown in Figures 10 and 11. These show the same order of convergence for MFEM with $\boldsymbol{RT}_0$ elements, the CVMFEM, and the MPFA, all with asymptotic convergence close to $O(h^2)$. The MPFA example is investigated further in [34]. The results show that the methods do not have reduced order of convergence on this relatively simple non-orthogonal grid compared to the orthogonal case.

9. Conclusions

Several locally conservative methods have been developed in recent years for equation (1), motivated by cases with irregular grids and anisotropic, discontinuous heterogeneous permeability. Perhaps not surprisingly, they are built on related foundations. The present investigation of these relationships should facilitate understanding of the literature and of the behavior of these methods.

All of the methods studied here can show second-order convergence of pressures and fluxes in problems with sufficiently smooth solutions, and sufficiently regular grids. For these methods to obtain optimal-order convergence, a type of weak continuity of the pressure is an essential common property. When this is inherent in the basic form of the method, Lagrange multipliers representing pressures at permeability discontinuities are not necessary.

The standard lowest-order Raviart-Thomas ($\boldsymbol{RT}_0$) MFEM provides a natural and convenient base-case framework from which to define and relate these locally conservative methods. The CVMFEM can be written as a MFEM with different test functions, chosen in a manner that

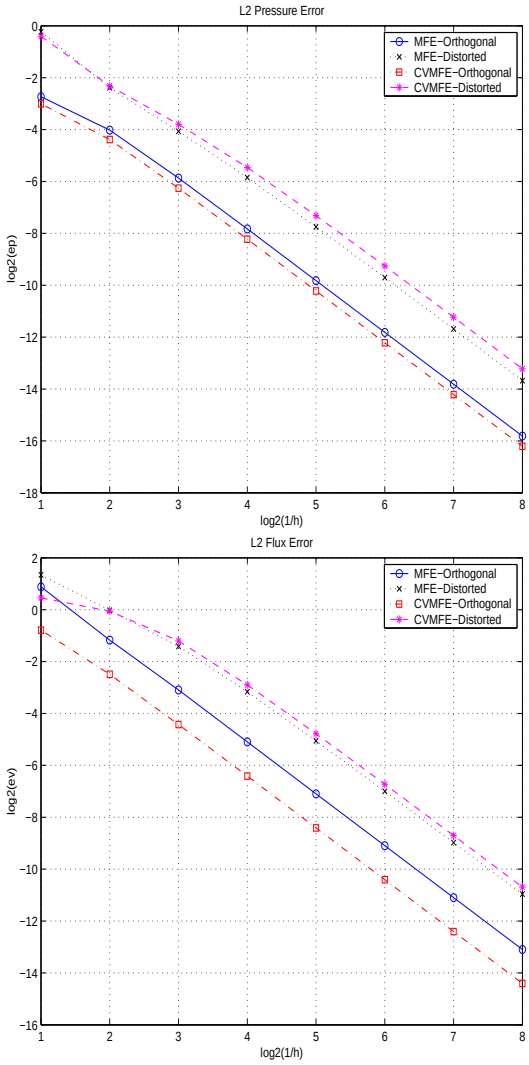

Figure 10. Numerical results for MFEM and CVMFEM

eliminates pressures at cell boundaries and assures weak pressure continuity. The SOM achieves the same result through a discrete adjoint-operator relation, and is equivalent to a MFEM with specific numerical integrations that are close to a mass-lumped MFEM or CVMFEM. All of these are "$\boldsymbol{K}^{-1}$ methods" that in some way use an inner product containing the inverse of the permeability tensor.

The expanded MFEM (EMFEM) is a "$\boldsymbol{K}$ method" that adds a pressure-gradient variable to the MFEM and has an inner product

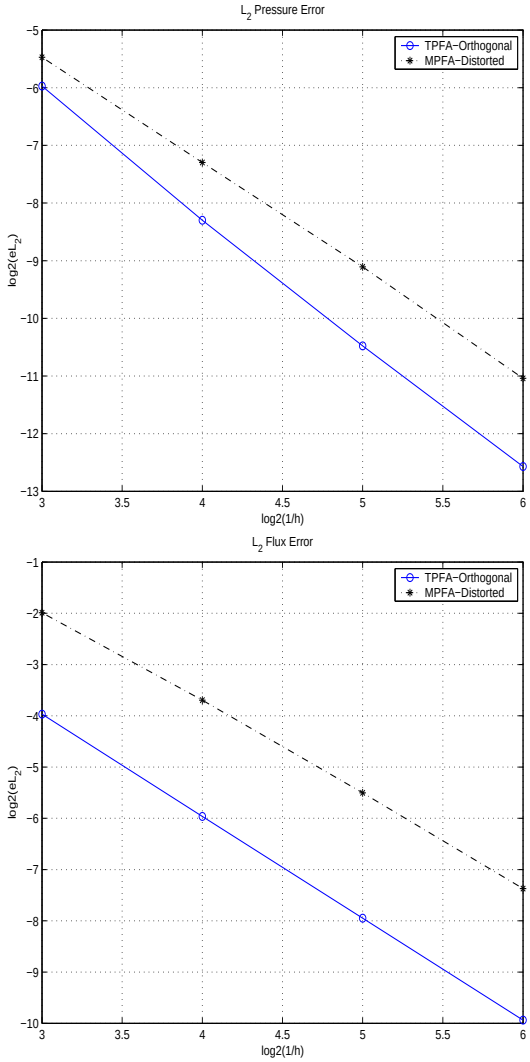

Figure 11. Numerical results for MPFA

containing the permeability tensor. When the same spaces are used for the pressure gradient and the flux, the EMFEM with certain numerical integrations leads to the ECCFDM, which needs Lagrange multipliers to enforce weak pressure continuity. If the pressure-gradient space is enlarged to allow discontinuous normal components, weak continuity follows without Lagrange multipliers. On orthogonal grids, with analogous numerical integrations and a splitting of edges into two parts, this produces the MPFA O-method.

It would be useful to study further the relationships between $\boldsymbol{K}$ methods and $\boldsymbol{K}^{-1}$ methods, considered for a simple parallelogram grid with MFEM/CVMFEM and the MPFA O-method in [28]. Extensions of some of the present MPFA-related findings to quadrilateral grids are reported in [35]. All of the methods extend to 3D, where the issues examined here become much more complex.

Acknowledgments

The authors thank John Wilson and Geir Terje Eigestad for help with numerical simulations. The second author was supported in part by National Science Foundation Grant Nos. DMS-0084438 and DMS-0222300.

References

1. M.G. Edwards, R.D. Lazarov, and I. Yotov (ed.): Special Issue on Locally Conservative Numerical Methods for Flow in Porous Media, Computational Geosciences **6**, Nos. 3–4, 2002.
2. F. Brezzi, M. Fortin: Mixed and Hybrid Finite Element Methods, Springer Series in Computational Mathematics, Vol. 15, Springer-Verlag, New York, 1991.
3. Z. Cai, J.E. Jones, S.F. McCormick, and T.F. Russell: Control-volume mixed finite element methods, Computational Geosciences **1**, pp. 289–315, 1997.
4. M. Berndt, K. Lipnukov, J.D. Moulton, and M. Shashkov: Convergence of mimetic finite difference discretizations of the diffusion equation, East-West J. Numer. Math. **9**, pp. 253–316, 2001.
5. J. Hyman, M. Shashkov and S. Steinberg: The numerical solution of diffusion problems in strongly heterogeneous non-isotropic materials, J. Comput. Phys. **132**, pp. 130–148, 1997.
6. T. Arbogast, M.F. Wheeler, and I. Yotov: Mixed finite elements for elliptic problems with tensor coefficients as cell-centered finite differences, SIAM J. Numer. Anal. **34**, pp. 828–852, 1997.
7. T. Arbogast, C.N. Dawson, P.T. Keenan, M.F. Wheeler, and I. Yotov: Enhanced cell-centered finite differences for elliptic equations on general geometry, SIAM J. Sci. Comput. **19**, pp. 404–425, 1998.
8. I. Aavatsmark, T. Barkve, Ø. Bøe, and T. Mannseth: Discretization on unstructured grids for inhomogeneous, anisotropic media. Part I: Derivation of the methods, SIAM J. Sci. Comput. **19**, pp. 1700–1716, 1998.
9. I. Aavatsmark, T. Barkve, Ø. Bøe, and T. Mannseth: Discretization on unstructured grids for inhomogeneous, anisotropic media. Part II: Discussion and numerical results, SIAM J. Sci. Comput. **19**, pp. 1717–1736, 1998.
10. I. Aavatsmark, T. Barkve, and T. Mannseth: Control-volume discretization methods for 3D quadrilateral grids in inhomogeneous, anisotropic reservoirs, SPE Journal **3**, pp. 146–154, 1998.
11. I. Aavatsmark: An introduction to multipoint flux approximations for quadrilateral grids, Computational Geosciences **6**, pp. 404–432, 2002.

12. M.G. Edwards and C.F. Rogers: Finite volume discretization with imposed flux continuity for the general tensor pressure equation, Computational Geosciences **2**, pp. 259–290, 1998.
13. M.G. Edwards and C.F. Rogers: A flux continous scheme for the full tensor pressure equation, Proc. 4th European Conference on the Mathematics of Oil Recovery, Vol. D, Røros, 1994.
14. R.L. Naff, T.F. Russell, and J.D. Wilson: Shape functions for velocity interpolation on general hexahedral cells, Computational Geosciences **6**, pp. 285–314, 2002.
15. J. Hyman, J. Morel, M. Shashkov, and S. Steinberg: Mimetic finite difference methods for diffusion equations, Computational Geosciences **6**, pp. 333–352, 2002.
16. J.A. Wheeler, M.F. Wheeler, and I. Yotov: Enhanced velocity mixed methods for flow in multiblock domains, Computational Geosciences **6**, pp. 315–332, 2002.
17. I. Mishev: Nonconforming finite volume methods, Computational Geosciences **6**, pp. 253–268, 2002.
18. S.H. Lee, P. Jenny, and H.A. Tchelepi: A finite-volume method with hexahedral multi-block grids for modeling flow in porous media, Computational Geosciences **6**, pp. 353–379, 2002.
19. G.T. Eigestad, I. Aavatsmark, and M. Espedal: Symmetry and M-matrix issues for the O-method on an unstructured grid, Computational Geosciences **6**, pp. 381–404, 2002.
20. M.G. Edwards: Unstructured, control-volume distributed, full-tensor finite-volume schemes with flow based grids, Computational Geosciences **6**, pp. 433–452, 2002.
21. R. Mosé, P. Siegel, P. Ackerer, and G. Chavent: Application of the mixed hybrid finite element approximation in a groundwater flow model: Luxury or necessity?, Water Resources Research **30**, pp. 3001–3012, 1994.
22. L.J. Durlofsky: Accuracy of mixed and control volume finite element approximations to Darcy velocity and related quantities, Water Resources Research **30**, pp. 965–973, 1994.
23. J. Wang and T. Mathew: Mixed finite element methods over quadrilaterals, in Proc. of the Third International Conference on Advances in Numerical Methods and Applications, I.T. Dimov et al., ed., World Scientific, pp. 203–214, 1994.
24. R.E. Ewing, M. Liu, and J. Wang: Superconvergence of mixed finite element approximation over quadrilaterals, SIAM J. Numer. Anal. **36**, pp. 772–787, 1999.
25. T.F. Russell and M.F. Wheeler: Finite element and finite difference methods for continuous flows in porous media, in The Mathematics of Reservoir Simulation, R.E. Ewing, ed., Frontiers in Applied Mathematics, Vol. 1, SIAM, Philadelphia, pp. 35–106, 1983.
26. P.A. Raviart and J.M. Thomas: A mixed finite element method for 2nd order elliptic problems, in Mathematical Aspects of Finite Element Methods, I. Galligani and E. Magenes, ed., Lecture Notes in Mathematics, Vol. 606, Springer-Verlag, New York, pp. 292–315, 1977.
27. G. Strang and G.J. Fix: An Analysis of the Finite Element Method, Wiley, New York, 1973.
28. T.F. Russell: Relationships among some conservative discretization methods, in Numerical Treatment of Multiphase Flows in Porous Media, Z. Chen et

al., ed., Lecture Notes in Physics, Vol. 552, Springer-Verlag, Heidelberg, pp. 267–282, 2000.
29. J.M. Nordbotten and I. Aavatsmark: Monotonicity conditions for control volume methods on uniform parallelogram grids in homogeneous media, submitted.
30. S. Chou, D.Y. Kwak, and K.Y. Kim: A general framework for constructing and analyzing mixed finite volume methods on quadrilateral grids: The overlapping covolume case, SIAM J. Numer. Anal. **39**, pp. 1170–1196, 2001.
31. M. Shashkov and S. Steinberg: Solving diffusion equations with rough coefficients in rough grids, J. Comput. Phys. **129**, pp. 383–405, 1996.
32. A.A. Samarskij: Theorie der Differenzenverfahren, Akademische Verlagsgesellschaft Geest & Poetig, Leipzig, 1984.
33. K. Aziz and A. Settari: Petroleum Reservoir Simulation, Applied Science Publishers, London, 1979.
34. G.T. Eigestad and R.A. Klausen: Convergence of multi-point flux approximation: Numerical experiments, in preparation.
35. R.A. Klausen: Convergence of multi-point flux approximations on quadrilateral grids, in preparation.

Appendix

A. Original Outline of the Support Operator Method

The Support Operator Method, SOM, is defined in the form of the operators $\mathcal{D}$ and $\mathcal{G}$, as

$$\boldsymbol{u}_{so} = \mathcal{G} p_{so}, \tag{59}$$

$$\mathcal{D}\boldsymbol{u}_{so} = G. \tag{60}$$

The operator $\mathcal{D}$ is a discrete version of the divergence. $\mathcal{G}$, which approximates $-\boldsymbol{K}\,\mathrm{grad}$, is described by three operators $\mathcal{S}$, $\mathcal{D}'$ and $\mathcal{M}$, such that $\mathcal{G} = \mathcal{S}^{-1}\mathcal{D}'\mathcal{M}$. If $\mathcal{S}$ is applied to both sides of (59),

$$\mathcal{S}\,\boldsymbol{u}_{so} = \mathcal{D}'\mathcal{M}\,p_{so}, \tag{61}$$

$$\mathcal{D}\,\boldsymbol{u}_{so} = G. \tag{62}$$

This is the form of the discrete equation actually found by the SOM methodology, and corresponds to MFEM with numerical integration. The discrete operators are constructed directly in the discrete scalar and vector function spaces, denoted by HC and $\mathcal{HS}$, respectively. HC is cell-centered, while $\mathcal{HS}$ is evaluated in terms of normal components on edges, corresponding to fluxes of the velocity. Two inner products for each of the discrete spaces are constructed, and will later be compared. The first are termed natural inner products, and are discrete versions

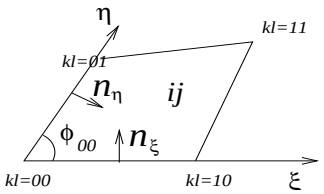

Figure 12. One SOM element, with the local coordinates for the element vertex $kl = 00$

of the classical $\mathcal{L}^2$ inner product for the scalar case, and the energy inner products, $(\boldsymbol{K}^{-1}\cdot,\cdot)$, for the vector functions. The scalar one is

$$(p,q)_{\mathrm{HC}} = \sum_{i,j=1}^{M-1,N-1} p_{ij} q_{ij}\, A_{ij},$$

where A_{ij} denotes the area of element ij. The vector natural inner product is more complex. To operate on $\mathcal{HS}$ degrees of freedom, i.e., normal components on edges, a separate coordinate transformation for each element vertex is applied. This implies a change from an orthogonal Cartesian basis to a basis consisting of the two normal components of the edges adjacent to the vertex. If $(\,\cdot\,)_{xy}$ denotes functions in the orthogonal Cartesian coordinate system and $(\,\cdot\,)_{\xi\eta}$ functions in the new coordinate system, the coordinate transform can be described by

$$(\boldsymbol{A})_{\xi\eta} = \boldsymbol{G}_{kl}(\boldsymbol{A})_{xy},$$

where $\boldsymbol{G}_{kl}$ is the transformation matrix for the vertex kl, and consists of the normal components, $\boldsymbol{n}_\xi$ and $\boldsymbol{n}_\eta$ (see Figure 12):

$$(\boldsymbol{A})_{\xi\eta} = \begin{pmatrix} A\xi \\ A\eta \end{pmatrix} = \begin{pmatrix} (\boldsymbol{A})_{xy}\cdot\boldsymbol{n}_\xi \\ (\boldsymbol{A})_{xy}\cdot\boldsymbol{n}_\eta \end{pmatrix} = (\boldsymbol{n}_\xi, \boldsymbol{n}_\eta)^T (\boldsymbol{A})_{xy}.$$

The $\mathcal{HS}$ natural inner product can now be defined by

$$(\boldsymbol{A},\boldsymbol{B})_{\mathcal{HS}} = \sum_{i,j=1}^{M-1,N-1} \sum_{k,l=0}^{1} (\boldsymbol{A}_{kl}^{ij})_{\xi\eta}^T (\boldsymbol{G}_{kl}^{ij})^{-T} \boldsymbol{K}_{ij}^{-1} (\boldsymbol{G}_{kl}^{ij})^{-1} (\boldsymbol{B}_{kl}^{ij})_{\xi\eta} A_{kl}^{ij}.$$

Here A_{kl}^{ij} is the area related to the vertex kl, such that $\sum_{kl} A_{kl}^{ij} = A_{ij}$. The area A_{kl}^{ij} equals half the area of the triangle in element ij which contains the angle ϕ_{kl} of vertex kl. Since the dot product is invariant under rotation, if the permeability is isotropic, $\boldsymbol{K} = k\mathbf{I}$, then $\boldsymbol{G}_{kl}$ depends only on the angle of the corner ϕ_{kl},

$$\boldsymbol{G}_{kl} = \begin{pmatrix} 1 & 0 \\ -\cos(\phi_{kl}) & \sin(\phi_{kl}) \end{pmatrix}.$$

Define $\boldsymbol{T} = \boldsymbol{G}^{-T}\boldsymbol{K}^{-1}\boldsymbol{G}^{-1}$; then

$$\boldsymbol{T}_{kl} = \frac{k^{-1}}{\sin^2(\phi_{kl})}\begin{pmatrix} 1 & \cos(\phi_{kl}) \\ \cos(\phi_{kl}) & 1 \end{pmatrix}.$$

This means for instance that,

$$\begin{aligned}(\boldsymbol{A})_{\xi\eta}^T\boldsymbol{G}^{-T}\boldsymbol{K}^{-1}\boldsymbol{G}^{-1}(\boldsymbol{B})_{\xi\eta} &= (\boldsymbol{A})_{\xi\eta}^T\boldsymbol{T}(\boldsymbol{B})_{\xi\eta} \\ &= \frac{A\xi B\xi + A\eta B\eta + (A\xi B\eta + A\eta B\xi)\cos(\phi)}{\sin^2(\phi)}.\end{aligned}$$

For a full permeability tensor the transformation will depend on the xy-coordinate system. Since the goal is to define discrete operators, another scalar and vector inner product are defined for comparison. These are termed formal inner products and can roughly be described as accumulation of the multiplied discrete functions. The formal inner product for the scalar functions is defined as

$$[p, q]_{\mathrm{HC}} = \sum_{i,j=1}^{M-1,N-1} p_{ij}q_{ij}.$$

For the vector functions it is

$$[\boldsymbol{A}, \boldsymbol{B}]_{\mathcal{HS}} = \sum_{i,j=1}^{M,N-1} A\xi_{ij}B\xi_{ij} + \sum_{i,j=1}^{M-1,N} A\eta_{ij}B\eta_{ij}.$$

The relationships between the natural and formal inner products are

$$(p, q)_{\mathrm{HC}} = [\mathcal{M}p, q]_{\mathrm{HC}}, \qquad \text{and} \qquad (\boldsymbol{A}, \boldsymbol{B})_{\mathcal{HS}} = [\mathcal{S}\boldsymbol{A}, \boldsymbol{B}]_{\mathcal{HS}}.$$

From these relationships, the operators $\mathcal{M}$ and $\mathcal{S}$ can be found. The main assumption behind SOM is existence of a discrete dual operator $\mathcal{D}^*$ in the natural inner product such that

$$(\mathcal{D}\boldsymbol{u}, p)_{\mathrm{HC}} = (\boldsymbol{u}, \mathcal{D}^*p)_{\mathcal{HS}}. \tag{63}$$

Here $\mathcal{D}^* = \mathcal{G}$, and is the approximation of $-\boldsymbol{K}\,\mathrm{grad}$. Equation (63) can be considered as an approximation of

$$\int_\Omega \mathrm{div}\,\boldsymbol{u}\,p\,d\boldsymbol{x} = -\int_\Omega (\boldsymbol{K}^{-1}\boldsymbol{u})^T\boldsymbol{K}\,\mathrm{grad}\,p\,d\boldsymbol{x},$$

where $(\cdot,\cdot)_{\mathrm{HC}}$ and $(\cdot,\cdot)_{\mathcal{HS}}$ can be seen as different numerical integration formulas. This is a version of Green's theorem, without the boundary terms that would lead to Lagrange multipliers. In terms of formal inner products, equation (63) reads

$$[\mathcal{D}\boldsymbol{u}, \mathcal{M}p]_{\mathrm{HC}} = [\boldsymbol{u}, \mathcal{S}\mathcal{D}^*p]_{\mathcal{HS}}.$$

Let the operator $\mathcal{D}'$ denote the adjoint of $\mathcal{D}$ in the formal inner product, so that

$$[\boldsymbol{u}, \mathcal{D}'\mathcal{M}p]_{\mathcal{HS}} = [\boldsymbol{u}, \mathcal{S}\mathcal{D}^* p]_{\mathcal{HS}}.$$

From this relationship it is possible to find $\mathcal{D}'$. Since the equation is true for all $\boldsymbol{u}$ and p,

$$\mathcal{D}'\mathcal{M} = \mathcal{S}\mathcal{D}^*,$$

and the discrete operator $\mathcal{G}$ is given by

$$\mathcal{G} = \mathcal{D}^* = \mathcal{S}^{-1}\mathcal{D}'\mathcal{M}.$$

B. Matrix from Section 7 Multi-Point Flux Approximation Control Volume Method

The matrices $\boldsymbol{A}, \boldsymbol{B}, \boldsymbol{C}$, and $\boldsymbol{D}$ are used to establish MPFA the original way in Section 7.

$$\boldsymbol{A} = \begin{bmatrix} \omega_{110} & 0 & 0 & \omega_{111} \\ \omega_{221} & \omega_{220} & 0 & 0 \\ 0 & \omega_{331} & \omega_{330} & 0 \\ 0 & 0 & \omega_{441} & \omega_{440} \end{bmatrix}, \tag{64}$$

$$\boldsymbol{B} = \begin{bmatrix} -\omega_{110} - \omega_{111} & 0 & 0 & 0 \\ 0 & -\omega_{220} - \omega_{221} & 0 & 0 \\ 0 & 0 & -\omega_{330} - \omega_{331} & 0 \\ 0 & 0 & 0 & -\omega_{440} - \omega_{441} \end{bmatrix}, \tag{65}$$

$$\boldsymbol{C} = \begin{bmatrix} \omega_{121} & \omega_{120} & 0 & 0 \\ 0 & \omega_{231} & \omega_{230} & 0 \\ 0 & 0 & \omega_{341} & \omega_{340} \\ \omega_{410} & 0 & 0 & \omega_{411} \end{bmatrix}, \tag{66}$$

$$\boldsymbol{D} = \begin{bmatrix} 0 & -\omega_{120} - \omega_{121} & 0 & 0 \\ 0 & 0 & -\omega_{230} - \omega_{231} & 0 \\ 0 & 0 & 0 & -\omega_{340} - \omega_{341} \\ -\omega_{410} - \omega_{411} & 0 & 0 & 0 \end{bmatrix}. \tag{67}$$

The matrices given next are used in Section 7.1 to find the connection between MPFA and EMFEM. The matrices are associated with an element E; see Figure 8.

$$\boldsymbol{M} = \begin{bmatrix} k_x^E & 1/2\, k_{xy}^E & 0 & 1/2\, k_{xy}^E \\ 1/2\, k_{xy}^E & k_y^E & 1/2\, k_{xy}^E & 0 \\ 0 & 1/2\, k_{xy}^E & k_x^E & 1/2\, k_{xy}^E \\ 1/2\, k_{xy}^E & 0 & 1/2\, k_{xy}^E & k_y^E \end{bmatrix}, \tag{68}$$

$$\boldsymbol{N} = \begin{bmatrix} k_x^E & 0 & k_{xy}^E & 0 & 0 & 0 & 0 & 0 \\ 0 & k_x^E & 0 & 0 & 0 & 0 & k_{xy}^E & 0 \\ k_{xy}^E & 0 & k_y^E & 0 & 0 & 0 & 0 & 0 \\ 0 & 0 & 0 & k_y^E & k_{xy}^E & 0 & 0 & 0 \\ 0 & 0 & 0 & k_{xy}^E & k_x^E & 0 & 0 & 0 \\ 0 & 0 & 0 & 0 & 0 & k_x^E & 0 & k_{xy}^E \\ 0 & k_{xy}^E & 0 & 0 & 0 & 0 & k_y^E & 0 \\ 0 & 0 & 0 & 0 & 0 & k_{xy}^E & 0 & k_y^E \end{bmatrix}, \tag{69}$$

$$\boldsymbol{P} = \frac{1}{2} \begin{bmatrix} 1 & 1 & 0 & 0 & 0 & 0 & 0 & 0 \\ 0 & 0 & 1 & 1 & 0 & 0 & 0 & 0 \\ 0 & 0 & 0 & 0 & 1 & 1 & 0 & 0 \\ 0 & 0 & 0 & 0 & 0 & 0 & 1 & 1 \end{bmatrix}. \tag{70}$$